

Dynamics of the Atlantic Marine Intertropical Convergence Zone

Hervé Giordani, Philippe Peyrillé

▶ **To cite this version:**

Hervé Giordani, Philippe Peyrillé. Dynamics of the Atlantic Marine Intertropical Convergence Zone. Journal of Geophysical Research: Atmospheres, 2022, 127, 10.1029/2021JD036392 . insu-03863746

HAL Id: insu-03863746

https://insu.hal.science/insu-03863746

Submitted on 21 Nov 2022

HAL is a multi-disciplinary open access archive for the deposit and dissemination of scientific research documents, whether they are published or not. The documents may come from teaching and research institutions in France or abroad, or from public or private research centers.

L'archive ouverte pluridisciplinaire **HAL**, est destinée au dépôt et à la diffusion de documents scientifiques de niveau recherche, publiés ou non, émanant des établissements d'enseignement et de recherche français ou étrangers, des laboratoires publics ou privés.



Distributed under a Creative Commons Attribution 4.0 International License

Check for updates

JGR Atmospheres

RESEARCH ARTICLE
10.1029/2021JD036392

Dynamics of the Atlantic Marine Intertropical Convergence Zone

Hervé Giordani[1] **and Philippe Peyrillé**[1]

[1]Centre National de Recherches Météorologiques, CNRM-CNRS, UMR3589, Météo-France, Toulouse, France

Key Points:

- Upward motions in the Atlantic Marine ITCZ are not resulting from latent heat release in the deep troposphere only
- Buoyancy fluxes, frontogenesis, and ageostrophic circulation are also key factors that force the ascent from the surface to the top
- The surface buoyancy flux is found to strongly influence the vertical velocity in the marine atmospheric boundary-layer, unlike the sea surface temperature

Correspondence to:
H. Giordani,
herve.giordani@meteo.fr

Citation:
Giordani, H., & Peyrillé, P. (2022). Dynamics of the Atlantic Marine Intertropical Convergence Zone. *Journal of Geophysical Research: Atmospheres*, *127*, e2021JD036392. https://doi.org/10.1029/2021JD036392

Received 21 DEC 2021
Accepted 26 JUL 2022

Author Contributions:
Conceptualization: Hervé Giordani
Formal analysis: Hervé Giordani
Investigation: Hervé Giordani
Methodology: Hervé Giordani
Resources: Philippe Peyrillé
Software: Hervé Giordani
Supervision: Philippe Peyrillé
Validation: Hervé Giordani
Visualization: Hervé Giordani
Writing – original draft: Hervé Giordani

© 2022. The Authors.
This is an open access article under the terms of the Creative Commons Attribution License, which permits use, distribution and reproduction in any medium, provided the original work is properly cited.

Abstract A generalized ω-equation is used to identify the contributions from different processes that force upward motions in the Atlantic Marine ITCZ (AMI) from a numerical mesoscale simulation of June 2010. This ω-equation separates the diabatic heating contributions, which lie at the core of the Weak Temperature Gradient (WTG) framework, from the dynamical terms. Three layers of atmosphere are found with different balance. In the Marine Atmospheric Boundary-Layer (MABL), the upward motions in the AMI are induced by the frontogenesis and buoyancy components, which are regulated by the ageostrophic adjustment due to the presence of thermal-wind imbalance. The balance of these three processes well captures the variability of the vertical velocity and the associated precipitation, meaning that boundary-layer processes play a central role in the AMI dynamics. In the layer [600–2,000 m], a zone of strong vertical wind-shear just above the MABL, the upward motions are induced by the ageostrophic adjustment and radiative components, which are counteracted by evaporation of convective precipitation. Above 2,000 m the ascending motions are driven by the deep convection heating, as expected by the WTG framework, and more surprisingly by the ageostrophic adjustment term within the Tropical Easterly Jet. Thanks to the use of the ω-equation, these results extend the current WTG framework to the boundary layer, where it is not expected to hold. In the free troposphere, the WTG framework only accounts for half of the AMI ascent, the other half being forced by the dynamical terms.

Plain Language Summary Upward motions in the Atlantic Marine ITCZ are generally explained as resulting from latent heat release associated with deep convection in the troposphere. This study shows that this approach is challenged by other processes on the vertical. In the lowest atmospheric layers, upward motions are driven by frontogenetic processes induced by wind convergence and by differential heating associated with the turbulent heat fluxes. In the middle troposphere, upward motions are controlled by ageostrophic adjustment, characterizing an unbalanced system, and radiative heating. In the deep troposphere, ascending motions are controlled by heating induced by the convective latent heat release, as expected by classic theories, but more surprisingly also by ageostrophic adjustment within the Tropical Easterly Jet. These results shows that dynamic forcings have an equivalent role to diabatic forcings in the production of upward motions within the ITCZ.

1. Introduction

The Atlantic Marine Intertropical Convergence Zone (AMI) is a central element in the tropical Atlantic climate system. The term AMI denotes the climatological envelope of tropical convective rain systems across the Atlantic ocean between West Africa and South America. The AMI seasonal migration is closely linked with seasonal rainfall variations over the adjacent land regions, giving it substantial societal significance (Bischoff & Schneider, 2014; Janicot et al., 2011; Schneider et al., 2014; Thorncroft et al., 2011). The AMI lies at the nexus of the trade wind systems of the Northern and Southern Hemispheres, which provide the moisture for the convection, respond to the associated convective heating, and interact with the underlying ocean to shape the climate of the larger tropical domain (Okumura & Xie, 2004; Peyrillé et al., 2016; Sultan & Janicot, 2003). Seasonal and interannual variability of the AMI and its extensions over the neighboring continents are closely associated with seasonal and interannual anomalies in the trade winds, sea surface temperature (SST), and the upper ocean circulation (Doi et al., 2012; Lamb et al., 1986; Mischell & Lee, 2022).

There are large gaps in our understanding of what controls the location and intensity of the global Intertropical Convergence Zone (ITCZ), and the AMI in particular. There is a close connection between the AMI and high tropical SST (≃29°C) but the relationship is not simple. The dynamical and physical properties of the surrounding atmospheric environment of the ITCZ are also important. To date there is no clear theory that combines these factors (SST, properties of the ITCZ and its environment) to provide a comprehensive understanding of the

21698996, 2022, 16, Downloaded from https://agupubs.onlinelibrary.wiley.com/doi/10.1029/2021JD036392 by Cochrane France, Wiley Online Library on [21/11/2022]. See the Terms and Conditions (https://onlinelibrary.wiley.com/terms-and-conditions) on Wiley Online Library for rules of use; OA articles are governed by the applicable Creative Commons License

21698996, 2022, 16, Downloaded from https://agupubs.onlinelibrary.wiley.com/doi/10.1029/2021JD036392 by Cochrane France, Wiley Online Library on [21/11/2022]. See the Terms and Conditions (https://onlinelibrary.wiley.com/terms-and-conditions) on Wiley Online Library for rules of use; OA articles are governed by the applicable Creative Commons License

climatological evolution of the AMI. The discrepancies in our knowledge are reflected in large biases in tropical SST and rainfall simulated by the majority of coupled global circulation models (Doi et al., 2012; Samanta et al., 2019; Voldoire et al., 2019; Wahl et al., 2009; Wang et al., 2021). Even models with prescribed SST often display a poor simulation of the AMI location and intensity, particularly in the Atlantic (Crespo et al., 2019). These problems affect our ability to describe, understand, and predict regional climate variability.

In ITCZ regions like in the AMI, low-level moisture convergence is often presented as the engine of upward motion and precipitation, so surface convergence might be an important factor determining where deep convection occurs at least at monthly time scale (Back & Bretherton, 2009). However, latent heating in deep convective systems also causes upward motion at smaller convective time scales ($\simeq$6 hr), which induces low-level convergence by continuity, thus this circular relationship offers no insights into the physical processes which generate low-level wind convergence and finally deep convection and heavy precipitation.

Numerous studies have investigated the influence of the SST on low-level wind convergence, deep convection, and associated precipitation in tropical regions (Back & Bretherton, 2009; Crespo et al., 2019; Diakhaté et al., 2018; Kang & Held, 2012; Meynadier et al., 2016) using a hierarchy of linear idealized models (Lindzen & Nigam, 1987; Neelin, 1989; Sobel & Neelin, 2006; Wang & Li, 1993; Zebiak, 1982) because they allow for a straightforward identification of the physical processes. These models control the surface wind convergence by SST-induced pressure adjustment (Lindzen & Nigam, 1987) and vertical momentum mixing (Chiang & Zebiak, 2000; McGauley et al., 2004; Stevens et al., 2002), so they have the merit of simplifying a complex problem. However, these simplifications give a distorted picture of what primitive equation models do and thus limit our understanding of the AMI dynamics and origins of biases of climate models in the tropics.

In the absence of a large horizontal gradient, the free troposphere is expected to follow the Weak Temperature Gradient (WTG) approximation (Sobel et al., 2001) relating the vertical profile of vertical velocity to the diabatic heating. The applicability of WTG has been discussed by Nie and Sobel (2016) with a simplified numerical protocol. This protocol couples a single column cloud resolving model, which solves the diabatic forcing, and a Quasi-Geostrophic (QG) ω-equation, which solves the vertical velocity. For scale disturbances greater than the Rossby radius of deformation (R_o), these authors have shown that the vertical velocity is controlled by the horizontal advection of vorticity, while for scale disturbances smaller than R_o, the vertical velocity is controlled by the temperature horizontal advection and diabatic heating. As a consequence, the WTG approximation is only valid for small scale disturbances and only when the temperature horizontal advection vanishes. Therefore, for intermediate scales around R_o, the system is not entirely controlled by diabatic (latent heat release of deep convection) or by adiabatic (advections of vorticity and temperature) processes, but by an infinite number of intermediate regimes including dynamical and thermodynamical processes. In the same line, Sobel and Neelin (2006) have shown that the deep convection results of boundary-layer temperature-convergence and high tropospheric latent heat release, which stand the system out of the WTG approximation.

Motivation of this study is to propose an extension of the Nie and Sobel's work in proceeding to an exhaustive and accurate identification of the processes involved in generation of wind convergence/divergence, namely generation of vertical velocity, in the AMI as an archetype of the ITCZ, by considering the system in its full complexity. In the free troposphere the weak temperature and pressure horizontal gradient allows linking the diabatic heating to the vertical velocity (Sobel et al., 2001) but it remains limited to the deep tropics and does not account for the forcing by the boundary-layer processes. In the present study particular attention is paid to processes in the marine atmospheric boundary layer (MABL) and refine their connections with the SST and turbulent surface heat fluxes. To achieve this objective, we evaluate the physical processes that stand behind vertical velocity in the primitive equations system, which is the common dynamical core of climate models. In this more general framework than linearized models cited above, the approach used in this study to infer the vertical velocity is based on the restoring of the thermal-wind balance because it links the mass and circulation fields. In this way, it will be possible to identify the respective roles of diabatic and adiabatic forcing in the production of vertical velocity.

According to the adiabatic Quasi-Geostrophic (QG) ω-equation, the vertical velocity motions are induced by convergence of the **Q**-vectors (Holton & Hakim, 2013; Hoskins et al., 1978). The QG ω-equation however neglects ageostrophic effects, friction and diabatic processes, particularly ones associated with SST and marine surface fluxes, which also affect vertical motions in the atmosphere, particularly in the MABL. Consequently, generalized ω-equations have been derived for the atmosphere and the ocean which include these processes (Giordani & Planton, 2000; Krishnamurti, 1968; Pauley & Nieman, 1992; Räisänen, 1995) to study factors affecting

21698996, 2022, 16, Downloaded from https://agupubs.onlinelibrary.wiley.com/doi/10.1029/2021JD036392 by Cochrane France, Wiley Online Library on [21/11/2022]. See the Terms and Conditions (https://onlinelibrary.wiley.com/terms-and-conditions) on Wiley Online Library for rules of use; OA articles are governed by the applicable Creative Commons License

vertical motions in the atmosphere (Stepanyuk et al., 2017) or ocean dynamics at fronts, filaments and eddies (Giordani & Caniaux, 2014; Giordani et al., 2006; Pascual et al., 2004; Ruiz et al., 2009).

In this study, the generalized ω-equation developed in Giordani and Planton (2000) is applied on a simulation of the regional Meso-NH model implemented in the tropical Atlantic. The month of June 2010 was chosen to be simulated because the SST and precipitation monthly anomalies reached 1.1°C and more than 1 mm day^{-1}, respectively, that represents more than two standard deviations from the mean over the period 1982–2016. This confirms the exceptional character of June 2010 and also of year 2010 (Marengo et al., 2013; Sodré & Filho, 2013). The generalized form of the ω-equation is applied to this simulation to diagnose the physical processes which generate vertical velocity in the AMI at hourly frequency. In that way, it is possible to propose a conceptual scheme of the AMI dynamics and to point out the mechanisms of coupling between the marine surface (SST, Flux) and wind convergence.

2. The Atmospheric Model Configuration for the AMI

The host model is the French community non-hydrostatic atmospheric simulation system Meso-NH (Lac et al., 2018; Lafore et al., 1998), which has been jointly developed by the Center National de Recherches Météorologiques [Météo-France and the Center National de la Recherche Scientifique (CNRS)] and the Laboratoire d'Aérologie (CNRS). This limited-area research model is based on the Durran (1989) modified anelastic system. It offers a complete physical package, including a fully interactive biosphere model, that is capable of doing simulations over a wide range of resolutions (100 km–1 m) for both real and idealized cases. It also provides powerful diagnostics to analyze model results in details.

For the present study, the following physical parameterizations have been activated: (a) the one-dimensional version of a turbulent scheme (Cuxart et al., 2000) based on diagnostic second-order moments and a turbulent kinetic energy equation and the mixing length of Bougeault and Lacarrère (1989); (b) a bulk microphysics scheme combining a three-class ice parameterization with Kessler's scheme for warm processes (Caniaux & Redelsperger, 1994; Pinty & Jabouille, 1998); (c) a convective scheme (Bechtold et al., 2001) adapted from Kain and Fritsch (1993); (d) the European Center for Medium-Range Weather Forecasts (ECMWF) operational radiation (Morcrette, 1991); and (e) the Interactions between the Surface-Biosphere-Atmosphere (ISBA) surface scheme of Mahfouf and Noilhan (1996). To improve the surface flux parameterization over ocean, the ECUME scheme based on multicampaigns has been activated (Belamari, 2005).

2.1. Initial and Boundary Conditions

Figure 1 presents the simulation domain extending from 63°W to 18°E in longitude and from 21°S to 21°N in latitude with a 10 km horizontal resolution representing 900 × 480 of grid points. In the vertical, the domain reaches a height of 22 km, using a stretched mesh from 10 m near the surface to 700 m in the upper troposphere and a sponge layer above 20 km to avoid wave reflection at the rigid upper boundary.

The atmospheric initial and lateral boundary conditions and SST are provided by the ERA-Interim (ERAi) reanalysis at 6-hourly frequency. June average SST and surface wind presented in Figure 1 highlight the presence of the equatorial cold tongue (≃22°C) due to the upwelling establishment in spring in the Gulf of Guinea and a maximum SST (>29°C) across the equatorial Atlantic basin and along the Brazilian coasts where the surface wind converges.

The lateral boundary conditions and SST are interpolated at each model time step (Δt = 30 s). The propagation of the lateral boundary conditions uses a method which modifies the prognostic equations in a zone close to the boundaries. This method combines a Newtonian nudging scheme (Davies, 1976) and a radiative propagation scheme for open boundaries (Klemp & Wilhelmson, 1978). The nudging technique imposes a relaxation of the prognostic variables toward large-scale variables over several rows of the simulation domain, and the radiative technique propagates the lateral boundary conditions by advection using a velocity normal to the boundaries (Carpenter, 1982).The number of relaxed rows from the lateral boundaries was kept equal to 4, and the phase speed of the radiative technique was kept equal to 30 ms^{-1}. This compromise led to a very clean behavior of the prognostic variables near the lateral boundaries.

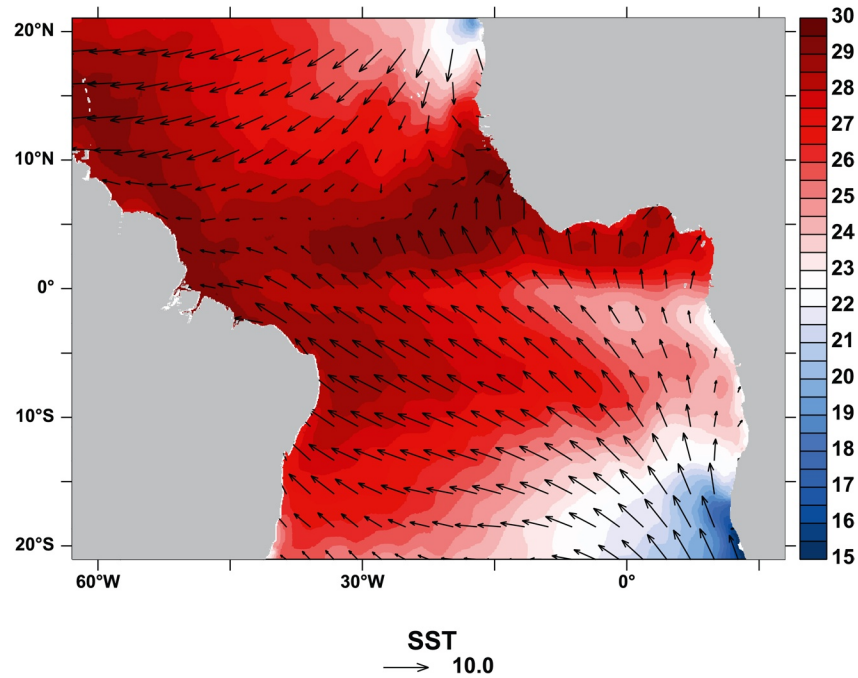


Figure 1. June 2010 averaged SST (°C) and surface wind (m s^{-1}).

The initialization of continental surface conditions is more complex as more than 20 surface (surface albedo, emissivity, fraction of vegetation, and leaf area index) and subsurface (type of soil, moisture conditions) properties need to be prescribed within the surface-biosphere scheme. For that initialization purpose, the ECOCLIMAP high-resolution land surface parameter database (Masson et al., 2003) is used, which is designed to initialize meteorological and climate models and initial moisture conditions are provided by the ERAi reanalyses. Starting from the above initial conditions, the model is integrated for 30 days from the 1 to 30 of June 2010. Atmospheric variables, diabatic and momentum fluxes and SST have been stored at hourly frequency in order to compute **Q**-vectors which force the generalized ω-equation.

3. Simulation of June 2010

Synoptic validations of the monthly mean precipitable water (PW), low-level vertical velocity (i.e., wind convergence), and monthly accumulated precipitation are presented in Figure 2. The Meso-NH and ERAi large structures of PW (Figures 2b and 2a) are close meaning that the model is realistic in simulating the humidity over troposphere. Because of its higher spatial resolution, the model simulates finer PW structures and latitudinal intrusions of PW associated with oscillations of the AMI in comparison with ERAi. Upward motions in the latitude belt [0−10°N] displayed by ERAi vertical velocity at 950 hPa (≃600 m, Figure 2c) are also present in the simulation (Figure 2d) but with a southward tilt and stronger intensities on the southern flank of the AMI. In response to high PW and vertical velocity, the simulated accumulated precipitation is maximum (≃800 mm, Figure 2f) in the eastern part of the basin and along the Brazilian coasts. This amount is consistent with TRMM data (Figure 2e), but the shape of the simulated precipitation is a little tilted southward in comparison with TRMM because of the vertical velocity forcing (Figure 2d). In addition, the model underestimates TRMM in the central part of the basin due to weaker upward vertical motion (Figure 2d). The high spot of precipitation around 9°S (Figure 2e) was due to the heavy precipitation event that occurred on 17 June (Silva et al., 2018).

Local validations of the model were performed versus in situ data collected on 15 buoys of the PIRATA network (Bourlès et al., 2019) during June 2010 and presented on Figure 3. The high correlation for SST between model and observation ($r = 0.96$) confirms that in situ data were assimilated into ERAi. This is an important point to investigate the role of the SST and surface flux on the wind convergence. The model/observation correlations obtained for the temperature ($T2m$), specific humidity ($Q2m$), sea level pressure (SLP) and the surface wind

21698996, 2022, 16, Downloaded from https://agupubs.onlinelibrary.wiley.com/doi/10.1029/2021JD036392 by Cochrane France, Wiley Online Library on [21/11/2022]. See the Terms and Conditions (https://onlinelibrary.wiley.com/terms-and-conditions) on Wiley Online Library for rules of use; OA articles are governed by the applicable Creative Commons License

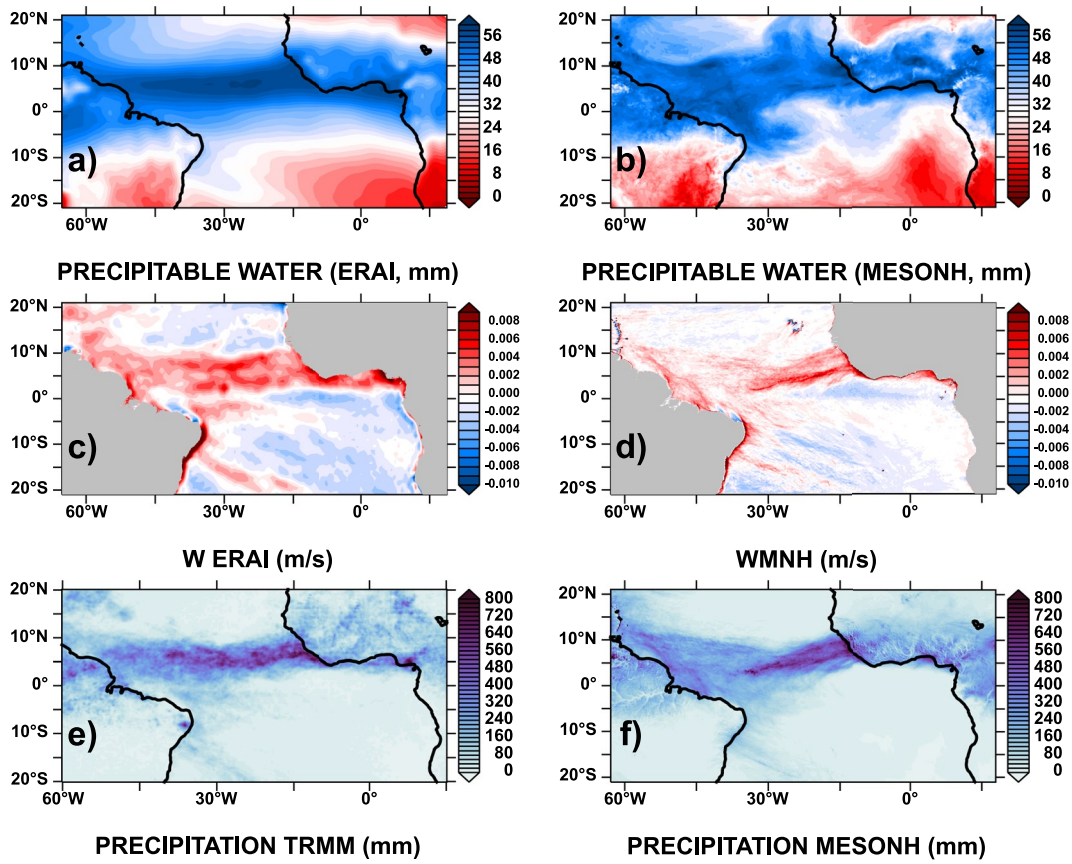


Figure 2. June 2010 averaged precipitable water (mm) (a) ERAi, (b) Meso-NH; Vertical velocity (m s^{-1}) (c) ERAi at 950 hPa, (d) Meso-NH averaged over the MABL (≃600 m) and Accumulated precipitation (mm) (e) TRMM, (f) Meso-NH.

($U10\ m$, $V10\ m$) are substantially high (0.9, 0.86, 0.9, 0.76, 0.86), respectively, and robust, because of the large number of data (≃8,000) used in computing these correlations.

The link of the sea level pressure (SLP) and precipitation rates on SST are estimated from the PIRATA buoy observations (Figures 4a and 4b) and model data (Figures 4c and 4d) interpolated at the buoys positions. The linear regressions in Figures 4a and 4b indicate that observations and model display similar negative main trends of SLP versus SST with correlation coefficients of $Cor_{obs} = 0.35$ and $Cor_{model} = 0.32$, respectively. These coefficients show a link of SLP to SST but it is moderate because of a large dispersion of SLP around these regressions. This result points out that the SST is not the only driver of the mass distribution, or pressure, which partly drives the circulation.

The precipitation rates collected by the rain gauges at the PIRATA buoys show a mode for SST around 29°C with extreme intensities ranging between 16 and 28 mm day^{-1}. Except the fact that observations are subject to errors, such extreme values are not present in the simulation because the model resolution ($\Delta x = 10$ km) needs to use a parametrization of deep convection. We can also note a skewness of the simulation distribution toward higher SSTs (≃30°C) compared to that of the observation (29°C). According to the Clausius-Clapeyron relationship, the higher saturation vapor pressure at 30°C than at 29°C could explain the precipitation decrease above 29°C in observations, while the occurrence of precipitation above 29°C in simulation could be the consequence of strong ascending vertical velocities because they force condensation.

The June average circulations in the AMI cross section at 20°W (see Figure 7a for the track of the vertical Section) for ERAi (Figure 5a) and Meso-NH simulation (Figure 5b) both highlight the strong ascending motions between 4°N and 10°N. The main ascending zone is well captured by Meso-NH between 4°N and 9°N. Meso-NH reproduces the associated deep meridional circulations, although the upper-level ascent is overestimated in the model. The shallow meridional circulation is also represented by the model south of 5°N in the [0–4,000 m]

21698996, 2022, 16, Downloaded from https://agupubs.onlinelibrary.wiley.com/doi/10.1029/2021JD036392 by Cochrane France, Wiley Online Library on [21/11/2022]. See the Terms and Conditions (https://onlinelibrary.wiley.com/terms-and-conditions) on Wiley Online Library for rules of use; OA articles are governed by the applicable Creative Commons License

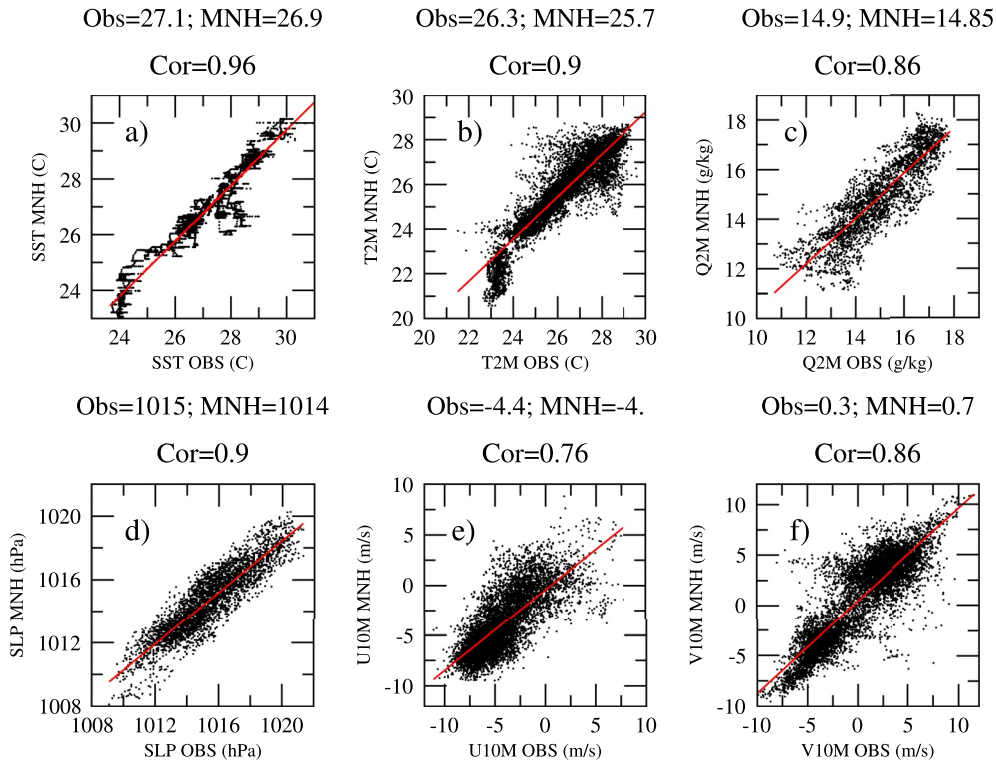


Figure 3. Scatterplots between observations (x axis) and simulation (y axis) data of the SST (°C), statistics: $\overline{Obs} = 27.1$, $\overline{MNH} = 26.9$, $Cor = 0.96$; Temperature at $z = 2$ m (T2M, °C), statistics: $\overline{Obs} = 26.3$, $\overline{MNH} = 25.7$, $Cor = 0.9$; specific humidity at $z = 2$ m (Q2M, g kg^{-1}), statistics: $\overline{Obs} = 14.9$, $\overline{MNH} = 14.85$, $Cor = 0.86$; Sea level pressure SLP (hPa), statistics: $\overline{Obs} = 1015$, $\overline{MNH} = 1014$, $Cor = 0.9$; zonal wind component at $z = 10$ m (U10 M, m s^{-1}) statistics: $\overline{Obs} = -4.4$, $\overline{MNH} = -4$, $Cor = 0.76$; and meridional wind component at $z = 10$ m (V10 M, m s^{-1}), statistics: S set means.

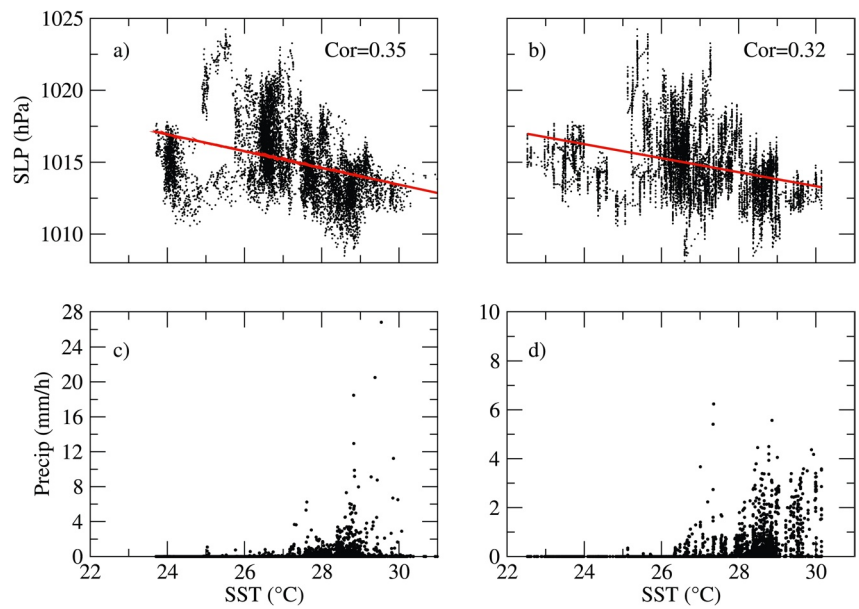


Figure 4. Sea level pressure (SLP, hPa) versus SST (°C) at PIRATA buoys (a) observations and (b) simulation. Red lines are the linear regression between SLP and SST. Precipitation rate (mm h^{-1}) versus SST (°C) at PIRATA buoys (c) observations and (d) simulation.

21698996, 2022, 16, Downloaded from https://agupubs.onlinelibrary.wiley.com/doi/10.1029/2021JD036392 by Cochrane France, Wiley Online Library on [21/11/2022]. See the Terms and Conditions (https://onlinelibrary.wiley.com/terms-and-conditions) on Wiley Online Library for rules of use; OA articles are governed by the applicable Creative Commons License

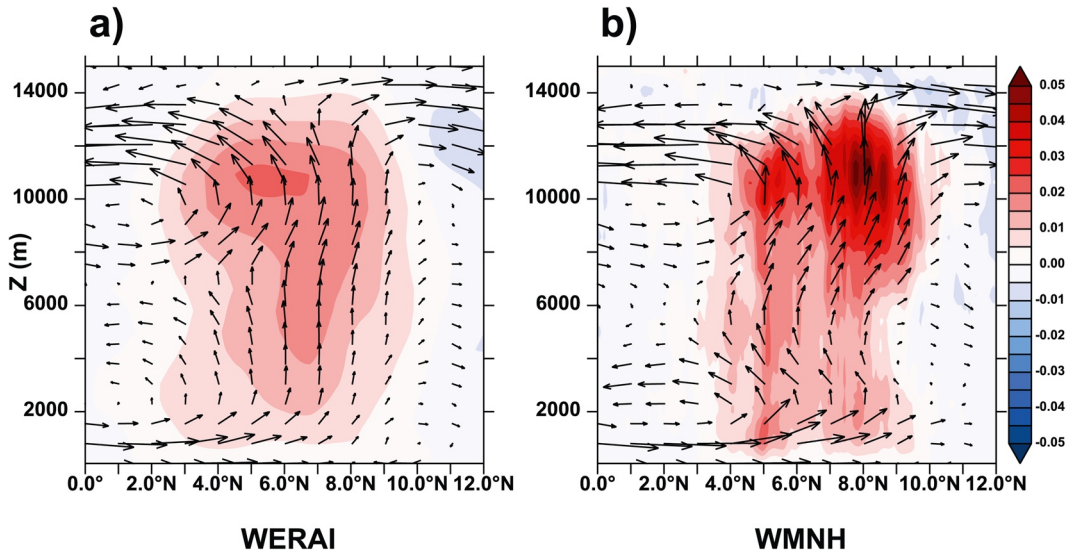


Figure 5. $[y - z]$ cross section at the longitude 20°W of vertical velocity (m s^{-1}) (a) ERAi (*WERAI*), (b) simulation (*WMNH*).

layer. It consists in a southerly inflow below 2,000 m, and a northerly return flow, which takes place in the layers [2,000–4,000 m] in Meso-NH and [2,000–6,000 m] in ERAi. The forcing terms of this shallow circulation is detailed in Section 4.3.2.

The superimpositions of the mean vertical velocity in the MABL (*WMNH*) on SST (Figure 6a), on turbulent surface heat flux (*FLUX* = *H* + *LE*; Figure 6b) and on MABL (defined from the potential temperature as: $\theta(z) - \theta(z = 10\text{ m}) \geq 0.2$°C Figure 6c) show good correspondence between the axis of maximum *WMNH* with highest SSTs (29°C) but not with the highest fluxes and highest MABL heights, as expected. In fact, this axis corresponds to minimum fluxes and minimum MABL heights indicating that the roles of these factors (SST, flux, MABL) on vertical velocity are poorly understood. In order to advance this understanding, the next Sections are devoted to identifying the physical processes generating vertical velocity and their links to the properties of the sea surface.

4. Processes of Vertical Motion

4.1. Generalized ω-Equation

In Giordani and Planton (2000) and Giordani et al. (2006), the full ageostrophic circulation $\vec{U}_{ag} = (u_{ag}, v_{ag}, w)$ is inferred from the material derivative of the Thermal-Wind Imbalance (**TWI**) defined as:

$$\begin{cases} TWI(x) = f\dfrac{\partial u}{\partial z} + \dfrac{g}{\theta}\dfrac{\partial \theta}{\partial y} = f\dfrac{\partial u_{ag}}{\partial z} \\ TWI(y) = f\dfrac{\partial v}{\partial z} - \dfrac{g}{\theta}\dfrac{\partial \theta}{\partial x} = f\dfrac{\partial v_{ag}}{\partial z} \end{cases} \quad (1)$$

where u, v, θ, and f are the zonal and meridional components of the wind, the potential temperature and the Coriolis parameter, respectively. The combination of the Lagrangian trend equation of **TWI** $\left(\frac{dT\vec{W}I}{dt}\right)$ and the mass conservation equation, generalizes the Hoskins et al. (1978) form of the vertical velocity, which is based on the quasi-geostrophic (QG) hypothesis, to the primitive equations system. The generalized form of the ω-equation used in this paper writes as follows:

$$\begin{cases} f^2\dfrac{\partial^2 w}{\partial z^2} + N^2\nabla_h^2 w = \vec{\nabla}.\vec{Q}_{tot} \\ \vec{Q}_{tot} = 2\vec{Q}_v + \vec{Q}_{vag} + \vec{Q}_{diab} + \vec{Q}_d + \vec{Q}_{tr} + \vec{Q}_\beta \end{cases} \quad (2)$$

21698996, 2022, 16, Downloaded from https://agupubs.onlinelibrary.wiley.com/doi/10.1029/2021JD036392 by Cochrane France, Wiley Online Library on [21/11/2022]. See the Terms and Conditions (https://onlinelibrary.wiley.com/terms-and-conditions) on Wiley Online Library for rules of use; OA articles are governed by the applicable Creative Commons License

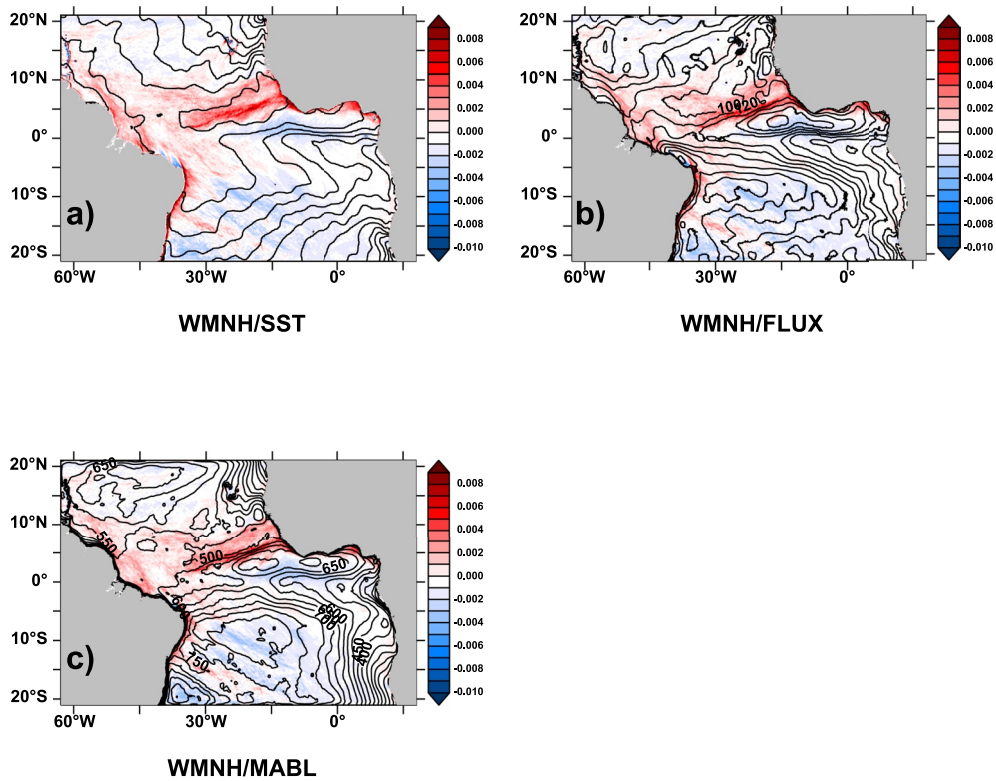


Figure 6. Superimposition of the June averaged boundary-layer vertical velocity (m s^{-1}) with (a) SST (°C), (b) sensible and latent heat flux (W m^{-2}), (c) MABL (m).

where $N^2 = \frac{g}{\theta}\frac{\partial \theta}{\partial z}$ is the Brünt Väisäila frequency. The six forcings of the ω-Equation 2 are the divergence of each **Q**-vector. Conceptually the ω-equation is a balance between the **Q**-vectors on the right-hand side of Equation 2 which produce the **TWI** and the vertical velocity w on the left-hand side of Equation 2 which tends to restore the thermal-wind balance. **Q**-vectors are the physical processes which are sources of vertical velocity and whose expressions are given below:

Frontogenesis: $\mathbf{Q}_v$

$$\begin{cases} Q_{vx} = -\frac{g}{\theta}\left(\frac{\partial u}{\partial x}\frac{\partial \theta}{\partial x} + \frac{\partial v}{\partial x}\frac{\partial \theta}{\partial y}\right) \\ Q_{vy} = -\frac{g}{\theta}\left(\frac{\partial v}{\partial y}\frac{\partial \theta}{\partial y} + \frac{\partial u}{\partial y}\frac{\partial \theta}{\partial x}\right) \end{cases}$$

Diabatic: $\mathbf{Q}_{diab}$

$$\begin{cases} Q_{diabx} = -\frac{g}{\theta}\frac{\partial}{\partial x}\left(\frac{\partial F_{diab}}{\partial z}\right) \\ Q_{diaby} = -\frac{g}{\theta}\frac{\partial}{\partial y}\left(\frac{\partial F_{diab}}{\partial z}\right) \end{cases}$$

Ageostrophic Shear: $\mathbf{Q}_{vag}$

$$\begin{cases} Q_{vagx} = f\left(\frac{\partial v}{\partial x}\frac{\partial u_{ag}}{\partial z} - \frac{\partial u}{\partial x}\frac{\partial v_{ag}}{\partial z}\right) \\ Q_{vagy} = f\left(\frac{\partial v}{\partial y}\frac{\partial u_{ag}}{\partial z} - \frac{\partial u}{\partial y}\frac{\partial v_{ag}}{\partial z}\right) \end{cases}$$

21698996, 2022, 16, Downloaded from https://agupubs.onlinelibrary.wiley.com/doi/10.1029/2021JD036392 by Cochrane France, Wiley Online Library on [21/11/2022]. See the Terms and Conditions (https://onlinelibrary.wiley.com/terms-and-conditions) on Wiley Online Library for rules of use; OA articles are governed by the applicable Creative Commons License

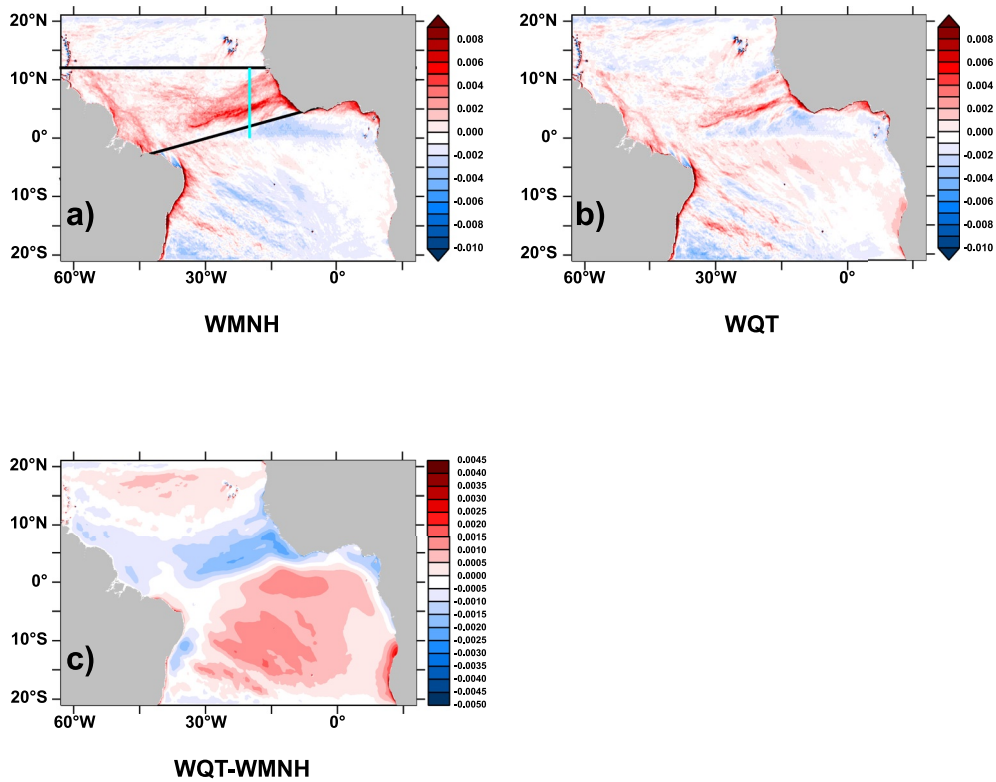


Figure 7. June averaged boundary-layer (a) simulated vertical velocity (*WMNH*, m s^{-1}). The black lines bound the AMI region which correspond to maxima of vertical velocity. The blue segment is the track of the vertical Section across the AMI where occur the most intense ascending motions. (b) Retrieved vertical velocity (*WQT*, m s^{-1}) after inversion of ω-Equation 2 and (c) difference *WQT* − *WMNH* (m s^{-1}).

Turbulent Momentum: $\mathbf{Q}_d$

$$\begin{cases} Q_{dx} = f\dfrac{\partial}{\partial z}\left(\dfrac{1}{\rho}\dfrac{\partial \tau_{yz}}{\partial z}\right) \\ Q_{dy} = -f\dfrac{\partial}{\partial z}\left(\dfrac{1}{\rho}\dfrac{\partial \tau_{xz}}{\partial z}\right) \end{cases}$$

Ageostrophic Trend: $\mathbf{Q}_{tr}$

$$\begin{cases} Q_{trx} = \dfrac{d}{dt}\left(f\dfrac{\partial v_{ag}}{\partial z}\right) \\ Q_{try} = -\dfrac{d}{dt}\left(f\dfrac{\partial u_{ag}}{\partial z}\right) \end{cases}$$

β Forcing: $\mathbf{Q}_\beta$

$$\begin{cases} Q_{\beta x} = -\beta v\dfrac{\partial v}{\partial z} \\ Q_{\beta y} = \beta v\dfrac{\partial u}{\partial z} \end{cases}$$

The diabatic **Q**-vector $\mathbf{Q}_{diab}$ includes the diabatic fluxes F_{diab} of deep convection, radiation, turbulent and shallow convection. In this study, we choose to merge the turbulent and shallow convection fluxes into a buoyancy flux ($F_b = \underbrace{\overline{w'\theta'_v}}_{turbulent} + \underbrace{w_c\theta_v}_{shallow\ convection}$) so that $\mathbf{Q}_{diab}$ has three components which are:

$$\vec{Q}_{diab} = \underbrace{\vec{Q}_b}_{buoyancy} + \underbrace{\vec{Q}_{conv}}_{deep\ convection} + \underbrace{\vec{Q}_{rad}}_{radiation}$$

21698996, 2022, 16, Downloaded from https://agupubs.onlinelibrary.wiley.com/doi/10.1029/2021JD036392 by Cochrane France, Wiley Online Library on [21/11/2022]. See the Terms and Conditions (https://onlinelibrary.wiley.com/terms-and-conditions) on Wiley Online Library for rules of use; OA articles are governed by the applicable Creative Commons License

21698996, 2022, 16, Downloaded from https://agupubs.onlinelibrary.wiley.com/doi/10.1029/2021JD036392 by Cochrane France, Wiley Online Library on [21/11/2022]. See the Terms and Conditions (https://onlinelibrary.wiley.com/terms-and-conditions) on Wiley Online Library for rules of use; OA articles are governed by the applicable Creative Commons License

and the dynamic **Q**-vector $\mathbf{Q}_{dyn}$ has five components which are:

$$\vec{Q}_{dyn} = \vec{Q}_v + \vec{Q}_{vag} + \vec{Q}_{tr} + \vec{Q}_d + \vec{Q}_\beta$$

- The frontogenesis **Q**-vector $\mathbf{Q}_v$—also named kinematic **Q**-vector—results of the product of the velocity gradient tensor with the temperature gradient. Physically it represents the temporal change in the horizontal temperature gradient induced by the horizontal wind field.
- The ageostrophic **Q**-vector $\mathbf{Q}_{vag}$ represents the stretching and reorientation of the preexisting vector **TWI** by the horizontal wind field. Components of **TWI** are the components of the ageostrophic horizontal pseudovorticity vector $\zeta_h^{ag} = (-TWI(y)/f, TWI(x)/f)$. The difference between horizontal pseudo-vorticity and vorticity is due to the terms $\partial_y w$ and $-\partial_x w$, respectively.
- The material derivative of **TWI** represented by $\mathbf{Q}_{tr}$ generalizes the ω-equation by taking into account the **TWI** storage and advection terms. As mentioned in Pietri et al. (2021), there has not yet been much study on this term.
- The turbulent momentum **Q**-vector $\mathbf{Q}_d$ takes into account the turbulent momentum flux $\vec{\tau}$ and modifies the vertical shear of horizontal wind by turbulence.
- The β **Q**-vector can be expressed as $\vec{Q}_\beta = \beta v \vec{\zeta}_{ph}$ (with $\vec{\zeta}_{ph}\left(-\frac{\partial v}{\partial z}, \frac{\partial u}{\partial z}\right)$ the horizontal pseudovorticity). As consequence, $\mathbf{Q}_\beta$ changes the vertical shear of the wind when the meridional wind (v) transports $\vec{\zeta}_{ph}$.

In the QG approximation, the ω-equation includes only the forcing term $\mathbf{Q}_v$, but considering the geostrophic wind and not the total wind (Hoskins et al., 1978). In this framework the thermal-wind balance destruction (or thermal-wind imbalance production) by the geostrophic wind is instantaneously restored by the ageostrophic circulation and the corresponding vertical velocity. A first step toward generalization is the adding of the ageostrophic shear term $\mathbf{Q}_{vag}$, corresponding to the contribution of ageostrophic advections, so-called Semi Geostrophic (SG) approximation. SG still assumes that the ageostrophic circulation restores the thermal-wind balance at any time, but it rectifies the forcing $\mathbf{Q}_v$ by considering the total wind instead of the geostrophic wind, as in the QG approximation. A last step is to use the generalized (or primitive) form which considers that the vertical velocity (ageostrophic circulation) does not restore at any time the thermal-wind balance. This introduces the trend term $\mathbf{Q}_{tr}$, which includes gravity-wave adjustments. In addition, the inclusion of diabatic fluxes in the temperature equation and turbulent momentum flux in the momentum equation introduces the forcing terms $\mathbf{Q}_{diab}$ and $\mathbf{Q}_d$, which are significant in the tropics. Finally $\mathbf{Q}_\beta$ refers to the advection of planetary vorticity by the meridional wind. The QG and SG approximation frameworks show how the **Q**-vectors are successively activated following the full primitive equation system. It is noteworthy that the WTG approximation, which relies on the vertical advection and diabatic heating balance, is a degenerate form of the QG ω-equation because it does take into account the stretching term $f^2\frac{\partial^2 w}{\partial z^2}$. Then the WTG approximation reduces the QG ω-Equation 2 to: $N^2\nabla_h^2 w = \vec{\nabla}.\vec{Q}_{diab}$.

In the primitive equation system, the **TWI** (or equivalently horizontal pseudo-vorticity) is produced by altering either the horizontal temperature gradient through the buoyancy $\mathbf{Q}_b$, convection $\mathbf{Q}_{conv}$, radiation $\mathbf{Q}_{rad}$ and frontogenesis $\mathbf{Q}_v$ forcings, either the vertical shear of the horizontal wind through the turbulent momentum $\mathbf{Q}_d$, ageostrophy $\mathbf{Q}_{vag}$, trend $\mathbf{Q}_{tr}$ and $\mathbf{Q}_\beta$ forcings. Formally, $L = f^2\frac{\partial^2}{\partial z^2} + N^2\nabla_h^2$ is an elliptic operator which has to be inverted to infer the vertical velocity from $w = L^{-1}[\nabla.\mathbf{Q}]$.

Due to the linear nature of Equation 2, its solution *WQT* can be represented as the superposition of these 8 components:

$$WQT = \underbrace{WQB + WQCONV + WQRAD}_{WQDIAB} + \underbrace{WQV + WQD + WQVAG + WQTR + WQBETA}_{WQDYN} \quad (3)$$

Inversion of Equation 2 gives access to the w-components associated with distinct process:

- Buoyancy flux: $\mathbf{Q}_b \rightarrow WQB$
- Radiation: $\mathbf{Q}_{rad} \rightarrow WQRAD$
- Convection: $\mathbf{Q}_{conv} \rightarrow WQCONV$
- Turbulent momentum flux: $\mathbf{Q}_d \rightarrow WQD$ so-called Ekman pumping
- Frontogenesis: $\mathbf{Q}_v \rightarrow WQV$

21698996, 2022, 16, Downloaded from https://agupubs.onlinelibrary.wiley.com/doi/10.1029/2021JD036392 by Cochrane France, Wiley Online Library on [21/11/2022]. See the Terms and Conditions (https://onlinelibrary.wiley.com/terms-and-conditions) on Wiley Online Library for rules of use; OA articles are governed by the applicable Creative Commons License

- Ageostrophy: $\mathbf{Q}_{vag} \rightarrow WQVAG$
- **TWI**-trend: $\mathbf{Q}_{tr} \rightarrow WQTR$
- β: $\mathbf{Q}_{\beta} \rightarrow WQBETA$

As indicated by Equation 2, the diabatic w-components WQB, $WQRAD$, and $WQCONV$ are controlled by the Laplacian of the vertical stretching of fluxes which represent the local warming ($\nabla^2 F < 0$) or cooling ($\nabla^2 F > 0$). WQD is related to the vertical shear of the momentum flux curl, namely the Ekman pumping. $WQTR$ explicitly contains the Lagrangian rate of change of the vertical shear of the ageostrophic vertical vorticity $\left(\zeta_z^{ag}\right)$. Consequently, this means that the generalized Equation 2 can also be interpreted in terms of the rate of change of ζ_z^{ag}. As mentioned in Viùdez et al. (1996), this term has to be considered for significant ageostrophic flow where the QG and SG approximations are not valid.

4.2. Method and Numerical Solution

The elliptic operator L is solved in the grid space based on the following iterative process. In the three-dimensional coordinate system (x, y, z), Equation 2 is discretized with centered second-order derivatives and is transformed as follows to be solved iteratively.

$$\begin{cases} A(k)w^n(i,j,k-1) + B(k)w^n(i,j,k) + C(k)w^n(i,j,k+1) = Y^{(n-1)}(i,j,k) \quad \text{Inversion} \rightarrow w_*^n \\ w^n(i,j,k) = (1-\alpha)w^{(n-1)}(i,j,k) + \alpha w_*^n \quad \text{Relaxation} \\ \text{where} \\ A(k) = \dfrac{f^2}{\Delta z^2} \\ B(k) = -2\left(\dfrac{f^2}{\Delta z^2} + N^2\left(\dfrac{1}{\Delta x^2} + \dfrac{1}{\Delta y^2}\right)\right) \\ C(k) = \dfrac{f^2}{\Delta z^2} \\ Y^{(n-1)}(i,j,k) = \vec{\nabla}.\vec{Q} - N^2\left(\dfrac{w^{(n-1)}(i-1,j,k) + w^{(n-1)}(i+1,j,k)}{\Delta x^2} + \dfrac{w^{(n-1)}(i,j-1,k) + w^{(n-1)}(i,j+1,k)}{\Delta y^2}\right) \end{cases} \tag{4}$$

where (i, j, k), Δx, Δy, Δz stand for indexes and grid mesh in the (x, y, z) directions, respectively, and n is the iteration step. A, B, C are the coefficients of the tridiagonal matrix which defines the vertical part of operator L. The horizontal part of L is represented by the crossed w-terms in $Y^{(n-1)}$. Inversion of this matrix on the vertical gives an estimation of the vertical velocity w_*^n at iteration n (first equation of System 4). Overrelaxation ($\alpha = 1.6$) is used to accelerate the convergence to provide the final solution after 60 iterations (second equation of System 4). System (4) has a unique solution if boundary conditions are known for all the domain. In this way, the solutions depend only on the accuracy of the **Q**-vector forcing.

The ability of the inversion method (Equation 4) to recover the vertical velocity of the model ($WMNH$) is evaluated by computing the monthly average of the w-components available at hourly frequency. These averages were computed in the tropical latitudes belt [5°S−15°N] because it includes the AMI, the Atlantic Cold Tongue (ACT) and the strong upward motions along the northern Brazilian coasts. The retrieved vertical velocity (WQT) includes the full forcing $\mathbf{Q}_{tot}$ of Equation 2.

The monthly fields $WMNH$ and WQT averaged over the MABL (≃600 m) point out that patterns of WQT are faithful to those of $WMNH$ (Figures 7a and 7b). In particular WQT well captures upward motions in the AMI and along the Northeastern coasts of Brazil, and downward motions which occur in the Gulf of Guinea and over the ACT. WQT also captures the wind convergence axis ($WMNH > 0$) in the south hemisphere which hit the Brazilian continent between 12°S and 5°S where heavy precipitation occurred especially in Recife on 17 June (Silva et al., 2018).

Biases of WQT versus $WMNH$ display a dipole of positive/negative values in both hemispheres and in the AMI, respectively (Figure 7c). Such biases (0.005 m s^{-1}) represent at maximum 50% of the magnitude of the vertical velocity (0.01 m s^{-1}) and show that the inversion method tends to underestimate upward and downward motions in and off the AMI, respectively. Such underestimates can be due to the lack of precision of **Q**-vector

21698996, 2022, 16, Downloaded from https://agupubs.onlinelibrary.wiley.com/doi/10.1029/2021JD036392 by Cochrane France, Wiley Online Library on [21/11/2022]. See the Terms and Conditions (https://onlinelibrary.wiley.com/terms-and-conditions) on Wiley Online Library for rules of use; OA articles are governed by the applicable Creative Commons License

forcings available at hourly frequency only and to the maximum number of iterations of the inversion algorithm (Equation 4).

Monthly mean vertical profiles of *WMNH* and *WQT* (Figure 8a) averaged over the AMI area, defined by the black lines in Figure 7a show that *WQT* has similar variations to *WMNH* but with weaker amplitudes. The bias reaches its maximum (0.001 m s^{-1}) in the layer [2500–10000 m] (Figure 8a). On the other hand, the standard deviations (STD) of *WMNH* and *WQT* (Figure 8b) are very close over the troposphere meaning a reasonable performance of the inversion algorithm. The standard deviations are one order of magnitude stronger than averages meaning a strong time variability of the vertical velocity. The root mean square (RMS) between *WQT* and *WMNH* does not exceed 25% of the standard deviation of *WMNH* meaning that the time variability of *WMNH* is fairly well captured by *WQT* on the vertical. These results confirm the good level of accuracy of the inversion algorithm (Equation 4). This gives some confidence to investigate the processes which produce vertical motions in the tropical Atlantic with a focus on the AMI.

4.3. *W*-Components

4.3.1. Marine Atmospheric Boundary Layer

This Section aims at identifying the physical processes responsible of upward motions which occur in the AMI and along the north Brazilian coasts (Figures 7a and 7b) through the **Q**-vectors decomposition of the vertical velocity. The monthly mean diabatic and dynamic components of the vertical velocity are averaged over the MABL and presented in Figures 9 and 10, respectively. The MABL height is diagnosed from the potential temperature criterion defined end of Section 3.

Regarding the diabatic w-components, upward motions are induced by *WQB* while downward motions are induced by *WQRAD* and *WQCONV* (Figure 9). The negative contribution of *WQCONV* corresponds to the evaporation of precipitation within the boundary layer in the deep convective regime. The negative/positive dipole of *WQRAD* associated with low-levels clouds and the positive/negative dipole of *WQB* in the western and eastern equatorial Atlantic, respectively, are fairly well collocated with SSTs close to 29°C, the ACT and the Current of Angola. This suggests a partial control of the SST on the diabatic w-components. This question is investigated in Section 4.4.

Regarding the dynamic *w*-components, the frontogenesis component *WQV* is by far the leading source of ascent motion up to 0.1 m s^{-1}, particularly along the West-East slant-oriented *w* axis and along the north Brazilian coasts (Figure 10). *WQV* is also active on the north flank of the AMI around 10°N (Figure 7a) but with much weaker intensities. *WQVAG* is negative and weakens *WQV* everywhere while *WQTR* weakens/reinforces *WQV* south/north of the West-East slant *w* axis. The significant intensities of *WQVAG* and *WQTR* indicate that **TWI** plays an important role in the AMI dynamics. *WQD* has more moderate intensities but cannot be neglected due to offsets between the other components. *WQD* induces downward motions in the core of the AMI at the exit of the African continent and in the Gulf of Guinea and upward motions in the western Atlantic and along the north and south flanks of the AMI. Finally the component *WQBETA* is neglected because it is at least one order of magnitude weaker than others.

Figure 11 displays the different terms of the balance, *WQBAL* obtained as: $WQBAL = WQBV + WQADJ$ (Figure 11c) where $WQBV = WQB + WQV$ (Figure 11a) and $WQADJ = WQVAG + WQTR$ (Figure 11b). It highlights that the boundary-layer vertical velocity in the AMI basically results from the competition between the upward forcings by the buoyancy (*WQB*) and by the frontogenesis (*WQV*) contributions on one hand and the subsidence contribution by the ageostrophic circulation (*WQVAG* and *WQTR*) on the other hand.

A complementary view is given by the decomposition of *WMNH* into its diabatic *WQDIAB* and dynamic *WQDYN* contributions which are shown in Figure 12. The opposition between *WQDIAB* and *WQDYN* indicates that the vertical velocity in the AMI and the ACT region mainly results of a competition between diabatic and dynamic processes and not of a constructive contributions of same signs. This suggests that diabatic and dynamic processes adjust themselves in order to minimize the **TWI**, in accordance with Le Chatelier's principle. *WQDYN* mainly explains the ascents patterns of *WMNH* from the African coasts to the Caribbeans north of 5°*N*, while *WQDIAB* mainly explains the ascents along the North Brazilian coasts from the equator to 10°N. As *WQV* and *WQADJ* control *WQDYN*, and *WQB* controls *WQDIAB*, we conclude that the wind convergence in the MABL

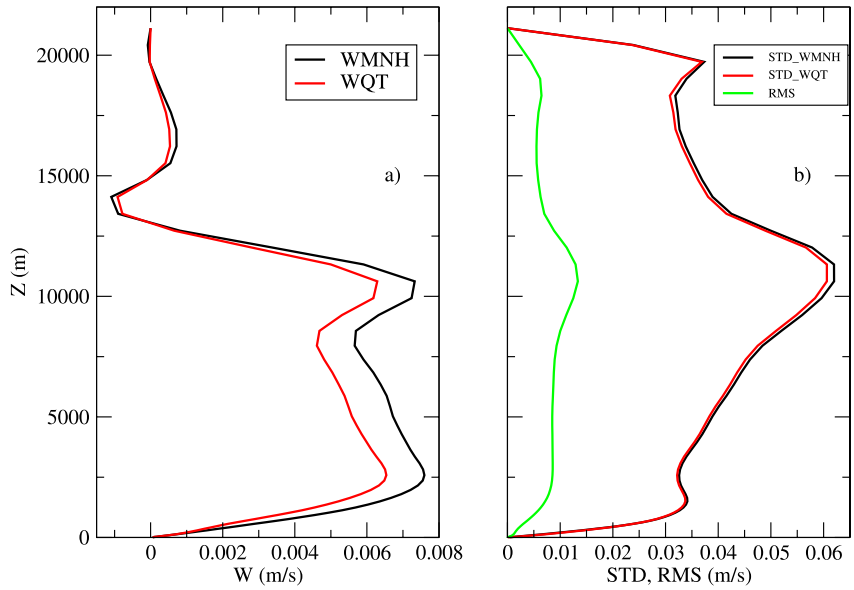


Figure 8. Using averages for June 2010 evaluated over the AMI (see Figure 7a for area), shown are (a) simulated vertical velocity *WMNH* (m s^{-1}) and retrieved vertical velocity *WQT* (m s^{-1}), (b) standard deviation (STD) of *WMNH* and *WQT* and root mean square (RMS) error (m s^{-1}).

mainly results from temperature and **TWI** deformations in the AMI and from the buoyancy fluxes in the western Atlantic. Note that the decrease of *WMNH* at the exit of Africa just north of the slant *w* axis is attributable to the weakening of the positive components *WQV* and *WQTR* which highlight the negative component *WQD*.

To summarize this analysis, meridional profiles across the AMI (see Figure 7a) in the MABL are presented in Figure 13. The SST increases from the equator to 4°N and is constant close to 29°C in the range [4−8°N] and decreases further to the north (Figure 13a). The accumulated precipitation (Figure 13b) displays broadly the same variations. This confirms that SST plays an important role in the atmosphere stability, but it is noteworthy that the peak of precipitation at 5°*N*, namely on the southern flanks of the AMI, is not collocated with the SST maximum but corresponds to meridional wind convergence (Figure 13c) and negative temperature gradient (Figure 13d) at 2 m high. These gradients produce intense positive *WQV* (not shown) driving *WQDYN* and finally the resulting total vertical velocity *WMNH* (Figure 13e). Interestingly the peak of precipitation around 5°N is associated with a dynamically driven ascent within the MABL. Precipitation in the range of latitudes [6°−9°N] are associated with more moderate *WMNH* which are mainly controlled by *WQB* (not shown) and finally *WQDIAB* (Figure 13e).

Temporal Variability. The Hovmöller diagram of *WMNH* through the AMI on the latitudinal cross section [0°−12°N] at the longitude 20°W (Figure 7a) highlights narrow lines of intense upward motion (Figure 14a) and precipitation rate (100 mm/day) (Figure 14b) which mark the south (more intense) and north (less intense) AMI flanks. The large latitudinal oscillations of these lines represent the spatiotemporal variability of the AMI which is first well captured by *WQV* and then by *WQB* (Figures 14c and 14d). *WQB* and *WQV* are the main sources of upward motion on the AMI flanks but have intensities larger than *WMNH*. The negative ageostrophic adjustment *WQADJ* (Figure 14d) leads to a budget $WQBAL = WQV + WQB + WQADJ$ (Figure 14f) in good accordance with *WMNH* (Figure 14a). This result confirms the previous monthly findings that the frontogenesis (*WQV*) and buoyancy flux (*WQB*) *w*-components are positive primary forcings which are regulated by the ageostrophic adjustment process (*WQADJ*) in the MABL of the AMI.

4.3.2. Vertical Structure

Tropospheric View. In the vertical cross section, *WMNH* displays two main branches of intense vertical motions up to 14,000 m high located at 5°N and 8°N (Figure 15a). These locations correspond to the southern and northern bounds of the AMI and define in some extent the envelope of the AMI. Two poles of maximum vertical velocity ($w \simeq 0.05$ m s^{-1}) are found around 11,000 m and two others of weaker intensity below 2,000 m. The

21698996, 2022, 16, Downloaded from https://agupubs.onlinelibrary.wiley.com/doi/10.1029/2021JD036392 by Cochrane France, Wiley Online Library on [21/11/2022]. See the Terms and Conditions (https://onlinelibrary.wiley.com/terms-and-conditions) on Wiley Online Library for rules of use; OA articles are governed by the applicable Creative Commons License

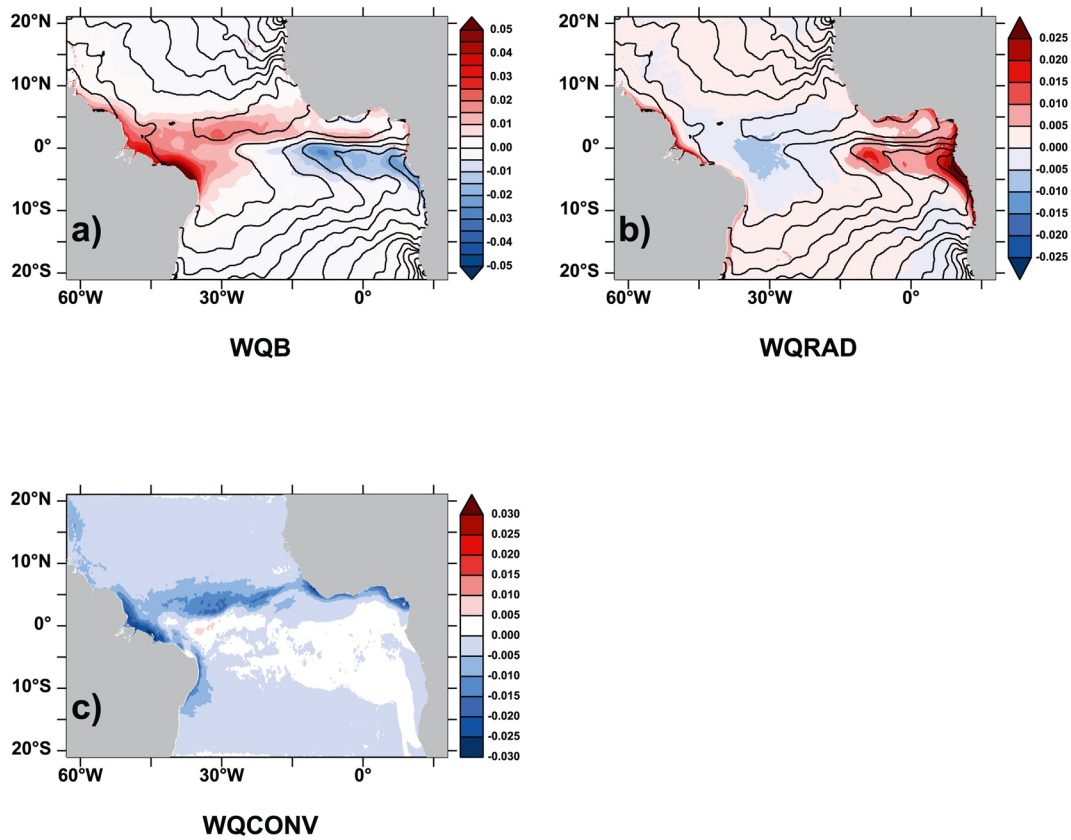


Figure 9. June boundary-layer averages of (a) buoyancy, (b) radiation superimposed with SST (°C), and (c) convection w-components (m s^{-1}).

wind vector (v, w) superimposed on the vertical cross-section highlights the presence of a shallow meridional circulation below 4,000 m on the south flank of the AMI. This shallow circulation is discussed below.

Opposition of the diabatic *WQDIAB* and dynamic *WQDYN* contributions to *WMNH* highlighted in the MABL (Figure 12) is confirmed in this vertical cross section (Figures 15b and 15c) up to 2,000 m approximately. Above the MABL, *WQDIAB* and *WQDYN* become constructive particularly in the southern (5°N) and northern (8°N) ascent branches of the AMI. Although the diabatic component is a structuring term in the peak convective area, it should be noted that surprisingly the dynamic part also contributes to the ascent and plays an important role in the construction of *WMNH*, particularly above 10,000 m. At such levels, the vertical shear of the easterly wind associated with the Tropical Easterly Jet (TEJ) is highly likely to be the cause of high *WQTR* intensities (not shown) but a deeper analysis is out of the scope of this study.

Now the temperature equation is used to estimate the respective contributions of the diabatic and dynamic terms to *WMNH* in the vertical cross section. These estimates were deduced from the stationarized temperature equation ($\partial\theta/\partial t = 0$), that is a reasonable assumption at monthly scale. In this thermodynamic framework, the diabatic contribution (*WWTG*) corresponds to the WTG approximation and the dynamic contribution (*WDYN*) is estimated as residual between *WMNH* and *WWTG*, as follows:

$$\begin{cases} WWTG = \dot{Q}_{diab} / \dfrac{\partial \theta}{\partial z} \\ WMNH = WWTG + WDYN \end{cases} \tag{5}$$

where $\dot{Q}_{diab}$ is the diabatic heating which includes radiative, turbulent, deep, and shallow convective forcings.

It can be seen in Figure 16 that *WWTG* is already a good estimate of *WMNH* in the free troposphere, however the dynamic component *WDYN* cannot be neglected in relation to *WWTG* showing that there is strong imbalance

21698996, 2022, 16, Downloaded from https://agupubs.onlinelibrary.wiley.com/doi/10.1029/2021JD036392 by Cochrane France, Wiley Online Library on [21/11/2022]. See the Terms and Conditions (https://onlinelibrary.wiley.com/terms-and-conditions) on Wiley Online Library for rules of use; OA articles are governed by the applicable Creative Commons License

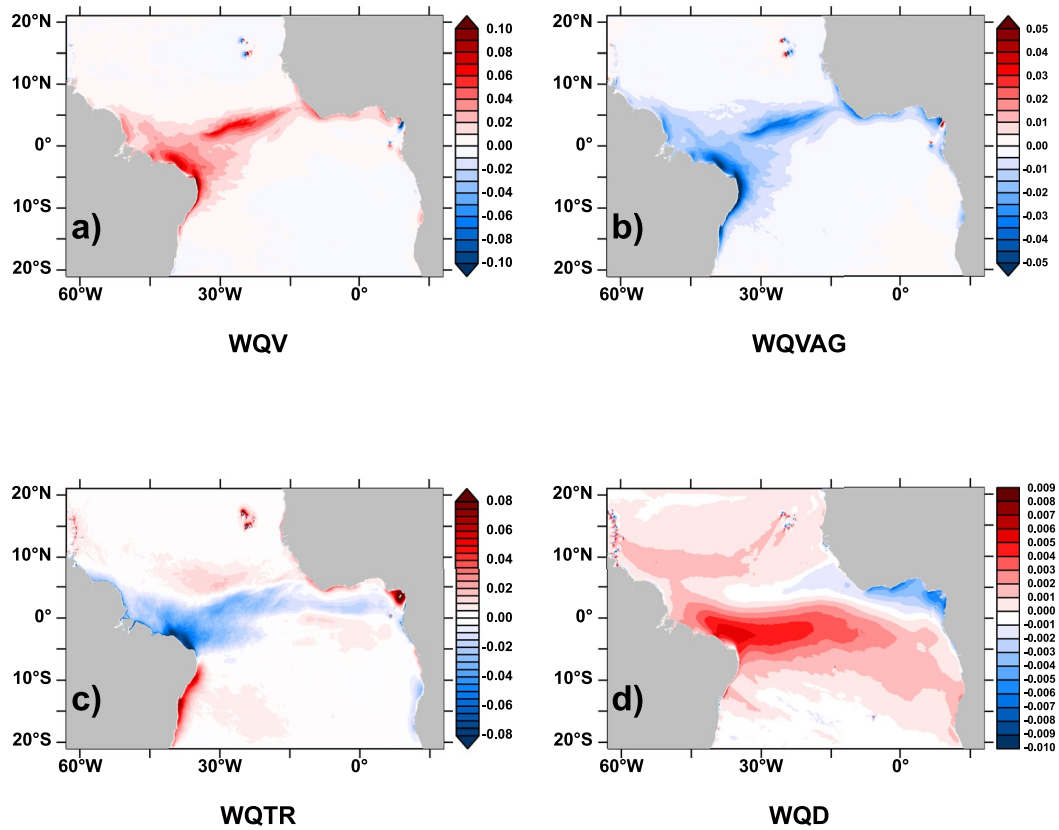


Figure 10. June boundary-layer averages of (a) frontogenesis, (b) ageostrophic, (c) trend, and (d) turbulent momentum w-components (m s^{-1}).

between the diabatic and dynamic forcings. In fact, the WTG approximation is intended to estimate the large-scale vertical velocity in the free atmosphere in order to force high-resolution cloud resolving models, which then resolve the fine-scale vertical velocity. In the boundary-layer the WTG method relaxes w to zero at the surface using a simple linear function (Herman & Raymond, 2014). It is therefore expected that WTG is no longer valid in the boundary-layer and for representing small-scale processes because it was not built for that. On the other hand, *WWTG* and *WDYN* have similar patterns to *WQDIAB* and *WQDYN* (Figures 15b and 15c), respectively, indicating that the thermodynamic and **Q**-vector approaches are consistent. The differences between *WWTG* and *WQDIAB* are partly attributed to the omission of the stretching term $f^2 \frac{\partial^2 w}{\partial z^2}$ in the WTG approximation. This result emphasizes that vertical motion does not only result from the balance between vertical temperature advection and diabatic forcing, as in the WTG approximation, but it also results from dynamical forcings, which are not present in the temperature equation, in accordance with Sobel and Neelin (2006) and Martin et al. (2016). However, a more robust assessment of the WTG approximation would be to have multiple validation realizations against a set of models. To our knowledge, the contribution of the dynamic part has not been so explicitly quantified in the literature and offers an interesting approach to extend current WTG theories outside the deep tropics.

Low-Levels Dynamics. Attention is now paid the vertical velocity and its components in the first 4,000 m (Figure 17). *WMNH* (Figure 17a) displays two relative maxima of vertical velocity around 1,500 m and 2,000 m at 5°N and 8°N, respectively, which are part of the two main ascent motions, shown on Figure 15a. Figure 17b points out that the strongest vertical velocity increases occur in the first 1,500 m, suggesting that boundary-layer processes are at stake in production of such divergence.

Two distinct layers are considered in the following because of different balances. The first layer lies in the MABL ($z < 600$ m) and the second one refers to the layer [600–2,000 m]. *WQV* (Figure 17c) and *WQB* (Figure 17f) are the two positive contributions to *WMNH* in the area of the south flank of the AMI around 5°N (Figure 17a). These strongest ascent contributions by the frontogenetic (*WQV*) and buoyancy (*WQB*) components (0.1 m s^{-1}) whose

21698996, 2022, 16, Downloaded from https://agupubs.onlinelibrary.wiley.com/doi/10.1029/2021JD036392 by Cochrane France, Wiley Online Library on [21/11/2022]. See the Terms and Conditions (https://onlinelibrary.wiley.com/terms-and-conditions) on Wiley Online Library for rules of use; OA articles are governed by the applicable Creative Commons License

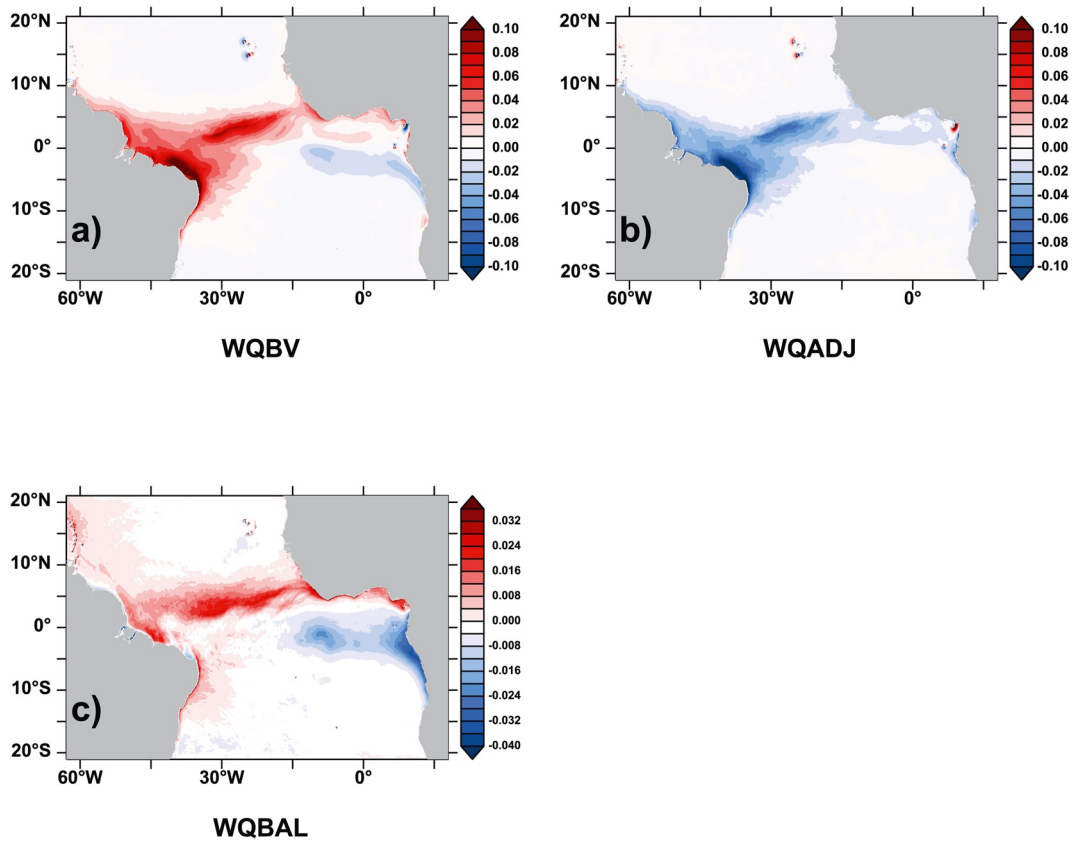


Figure 11. June boundary-layer averages w-components (m s^{-1}) of (a) $WQBV = WQB + WQV$, (b) $WQADJ = WQVAG + WQTR$, and (c) the budget $WQBAL = WQBV + WQADJ$.

joined contribution $WQBV = WQB + WQV$ (Figure 17i) is primarily balanced by $WQADJ$ (Figure 17d) (this confirms the balance in the MABL already shown in Figures 11a and 11b) and to a lesser extent by $WQCONV$ (Figure 17g) and by WQD (Figure 17e). Note that the high intensity of WQV in the MABL, particularly in the latitude range [4°−6°N], is consistent with the surface convergences of wind and temperature shown in Figures 13c–13e.

It is noteworthy to point out that deep convection induces downward motion ($WQCONV < 0$) in lower layers which is associated with evaporation of precipitation. The negative contribution of $WQCONV$ and WQD in the range of latitudes [5°−7°N] explains the local minimum of $WMNH$. On the northern flank of the AMI around 8°N, WQV and WQB have moderate intensities compared to the southern one and contribute to upward motion in

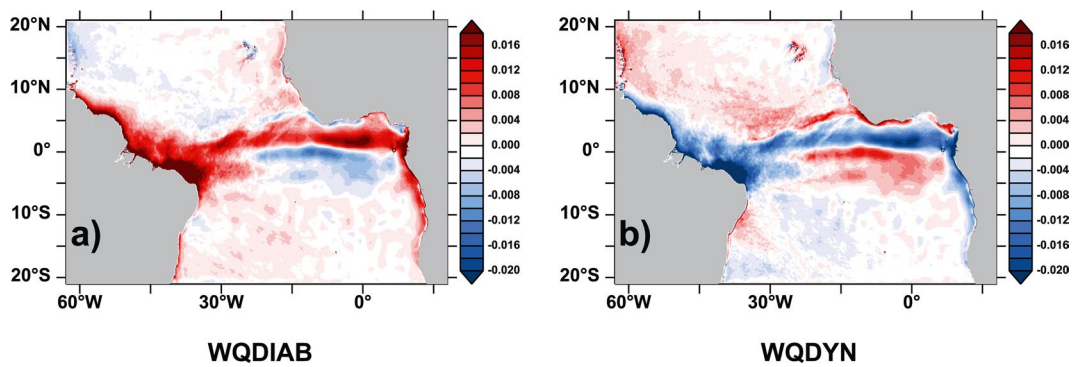


Figure 12. June boundary-layer averages of (a) diabatic ($WQDIAB = WQB + WQCONV + WQRAD$) and (b) dynamic ($WQDYN = WQV + WQVAG + WQTR + WQD + WQBETA$) w-components (m s^{-1}).

21698996, 2022, 16, Downloaded from https://agupubs.onlinelibrary.wiley.com/doi/10.1029/2021JD036392 by Cochrane France, Wiley Online Library on [21/11/2022]. See the Terms and Conditions (https://onlinelibrary.wiley.com/terms-and-conditions) on Wiley Online Library for rules of use; OA articles are governed by the applicable Creative Commons License

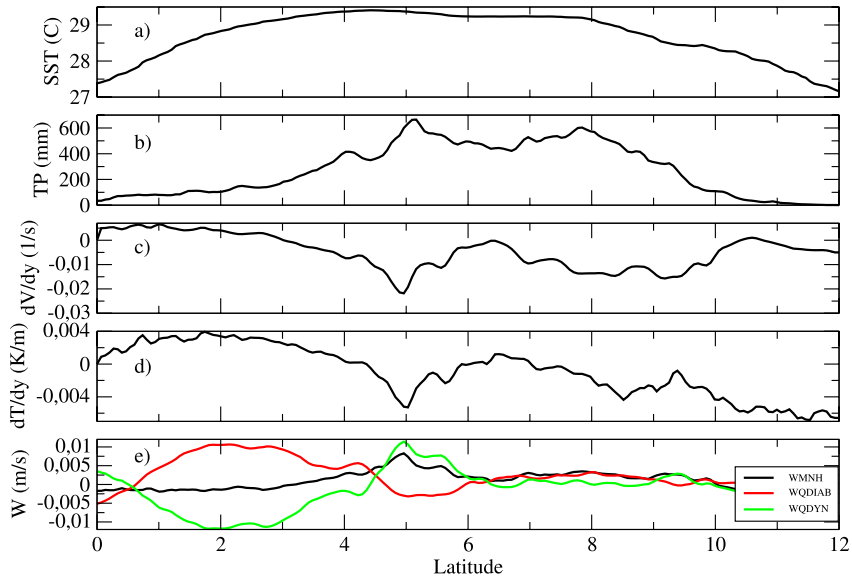


Figure 13. [$y - z$] cross section at the longitude 20°W of (a) SST (°C), (b) accumulated precipitation (mm), (c) meridional gradient of meridional wind ($\partial v/\partial y$, s^{-1}), (d) meridional gradient of temperature ($\partial\theta/\partial y$, K m^{-1}), (e) vertical velocity (m s^{-1}).

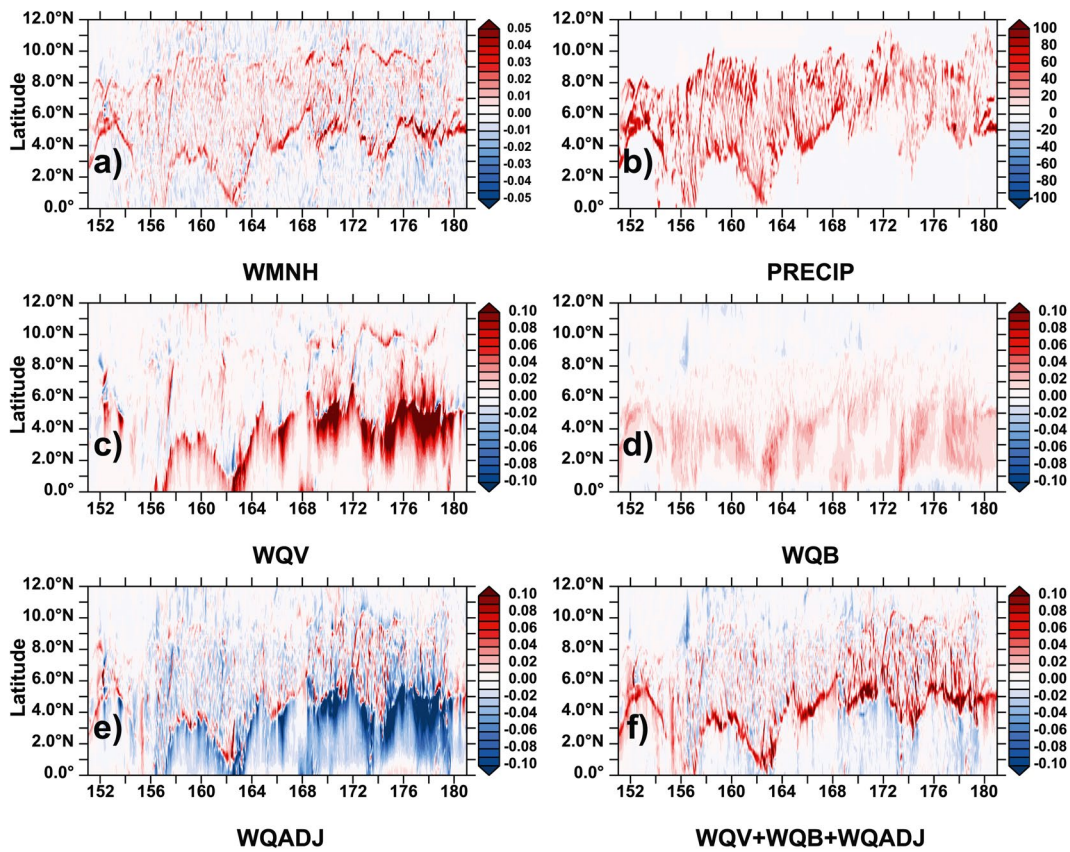


Figure 14. Hovmöller diagram across the AMI on the latitudinal cross section [0°−12°N] at the longitude 20°W of (a) simulated vertical velocity *WMNH* (m s^{-1}), (b) precipitation (mm day^{-1}), (c) frontogenesis (*WQV*), (d) buoyancy (*WQB*), (e) adjustment (*WQADJ* = *WQVAG* + *WQTR*), and (f) budget *WQV* + *WQB* + *WQADJ* *w*-components (m s^{-1}). *x* axis displays the Julian days (JD) between 1 June (JD = 151) to 30 June (JD = 181).

21698996, 2022, 16, Downloaded from https://agupubs.onlinelibrary.wiley.com/doi/10.1029/2021JD036392 by Cochrane France, Wiley Online Library on [21/11/2022]. See the Terms and Conditions (https://onlinelibrary.wiley.com/terms-and-conditions) on Wiley Online Library for rules of use; OA articles are governed by the applicable Creative Commons License

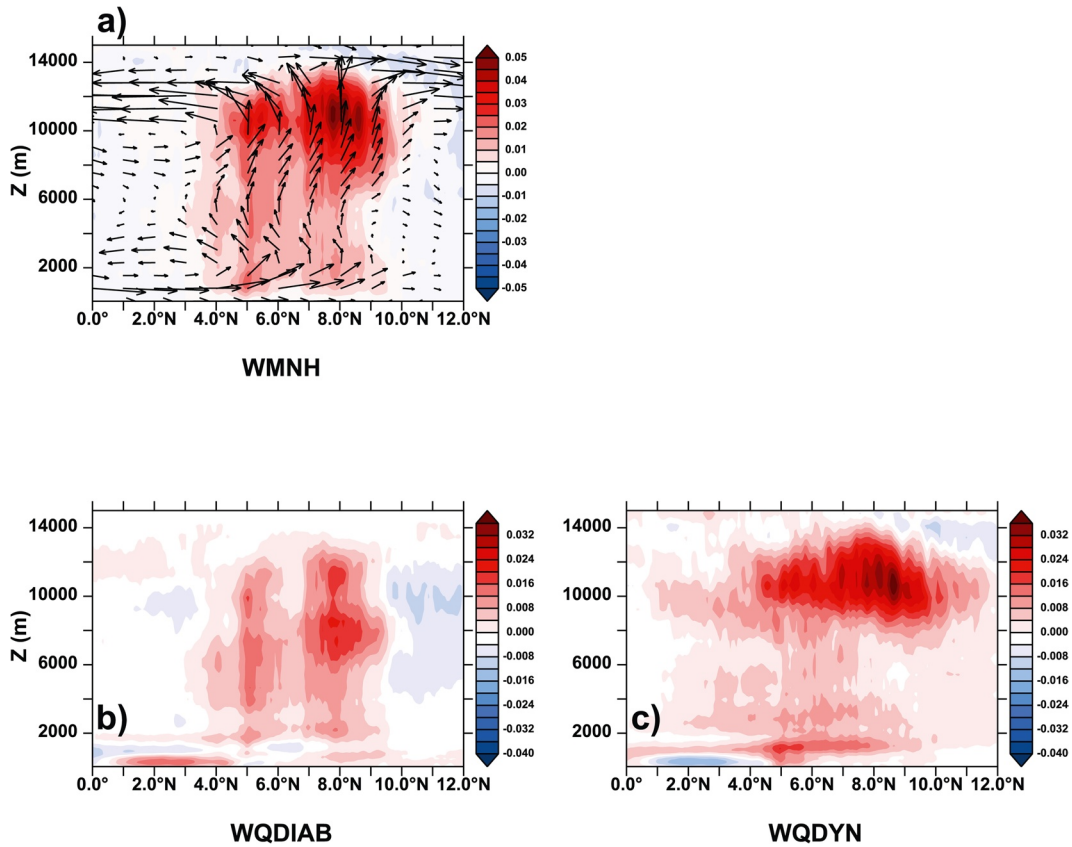


Figure 15. [$y - z$] cross section at the longitude 20°W of vertical velocity (m s^{-1}) (a) simulation (*WMNH*), (b) diabatic (*WQDIAB*), and (c) dynamic (*WQDYN*) *w*-components.

the same order of magnitude than *WQRAD* (Figure 17f) and *WQD*. Note that *WQD* is source of upward motions close to the equator.

Above the MABL in the layer [600–2,000 m], *WQADJ* (Figure 17d) and *WQRAD* (Figure 17h) become sources of ascent motions which are attributed to the vertical shear of the meridional wind at the MABL top (Figure 17i) and to low-levels clouds, respectively. Because of latent heat release the deep convection component *WQCONV* (Figure 17g) becomes positive in the layer [2,000–4,000 m] and prevails the diabatic component *WQDIAB* at higher levels (Figure 15b).

Figure 17i highlights the well-known tropical shallow meridional circulation described in Zhang et al. (2004) which consists of ascending motions at 5°N, a southerly inflow below 2,000 m, and a northerly return flow in the layer [2,000–4,000 m]. The fairly good spatial correspondence between the positive forcing *WQBV* (Figure 17i) with the southerly inflow convergence and the *WMNH* divergence in the MABL ($z < 600$ m) suggests that the engine of this shallow circulation is driven by diffusive and shallow convective heatings and frontogenesis. In the vertical wind-shear area [600–2,000 m], the positive components $WQADJ \simeq WQTR$; which results of the stretching of the ageostrophic vorticity; and *WQRAD* are grouped in the variable $WQRADJ = WQRAD + WQADJ$. It can be seen in Figure 17j that *WQRADJ* sustains the meridional wind convergence and thus the increase of *WMNH* above the MABL. In the layer [2,000–4,000 m] the decrease of *WMNH* forces the northerly return flow because of the collapse of *WQRAD* and *WQADJ* and moderate positive contribution of *WQCONV*.

Now the vertical structures of the *w*-components are investigated at the AMI scale. At each vertical level, the *w*-components are averaged over the domain which encompasses the strongest vertical velocities (see the domain in Figure 7a). The vertical distributions of the averaged *w*-components over the AMI domain (Figure 18) confirms the results obtained on the vertical section (Figure 17), in particular for the contributions of ascent motion.

To summarize this analysis, the meridional wind convergence and the associated upward motions in the first 2,000 m are generated by distinct processes which are:

21698996, 2022, 16, Downloaded from https://agupubs.onlinelibrary.wiley.com/doi/10.1029/2021JD036392 by Cochrane France, Wiley Online Library on [21/11/2022]. See the Terms and Conditions (https://onlinelibrary.wiley.com/terms-and-conditions) on Wiley Online Library for rules of use; OA articles are governed by the applicable Creative Commons License

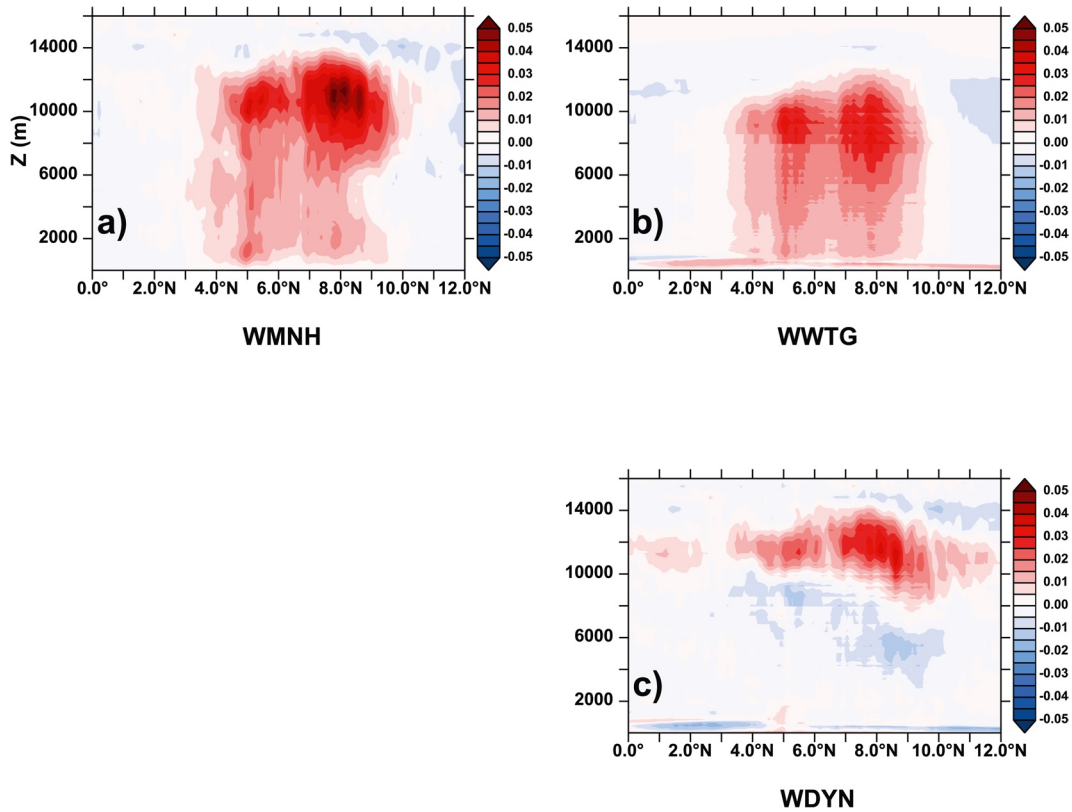


Figure 16. $[y - z]$ cross section at the longitude 20°W of vertical velocity (m s^{-1}) (a) simulation (*WMNH*), deduced from the temperature equation (b) diabatic (*WWTG*), (c) dynamic (*WDYN*) components.

- The frontogenesis *WQV* and buoyancy *WQB* *w*-components in the MABL ($z < 600$ m)
- The ageostrophic *WQADJ* and radiation *WQRAD* *w*-component in layer [600–2,000 m]

Finally in Figures 17 and 18, it can be seen that the combination of all processes are needed to retrieve faithfully the patterns of the total vertical velocity. This result points out that the vertical velocity in the AMI results of complex interactions between diabatic and dynamic processes.

4.4. Boundary-Layer Vertical Velocity Adjustment to the Marine Surface

In this section, we assess the role of the marine surface properties on the wind convergence (vertical velocity) in the MABL of the AMI. To estimate this connection, the time correlation computed at hourly frequency, of *WMNH* to the SST ($COR < WMNH, SST >$) is first shown Figure 19a. This correlation is weak and does not show a clear signature of the AMI excepted perhaps on the south and north flanks of the AMI where organized patterns emerge weakly. Consequently, SST does not seem to be a relevant surface parameter for controlling the temporal variability of the wind convergence in the MABL. However, the correlation of *WMNH* to the surface buoyancy flux (*FBUO*) ($COR < WMNH, FBUO >$) presented in Figure 19b shows positive values and organized patterns in the AMI and along the North Brazilian coasts. This result points out the significant link between *FBUO* and the circulation which indicates that the atmosphere rather responds to surface fluxes than to SST. Clearly, the correlation $COR < WQB, FBUO >$ gives the background to $COR < WMNH, FBUO >$ (Figure 19c) because *FBUO* is the surface boundary-condition of the buoyancy **Q**-vector $\mathbf{Q}_b$. High values of $COR < WQV, FBUO >$ are found on the south flank of the AMI and along the Guinea coasts where the temperature convergence is strong (Figure 19d). Correlations $COR < WQD, FBUO >$ (Figure 19e) and $COR < WQTR, FBUO >$ (Figure 19f) contribute to $COR < WMNH, FBUO >$ (Figure 19b) mainly on the north and south flanks of the AMI. To conclude the surface buoyancy flux *FBUO* imprints a control more efficient than SST on the vertical velocity in the MABL mainly through the buoyancy flux (*WQB*), frontogenesis (*WQV*), Ekman pumping (*WQD*), and **TWI** (*WQTR*) *w*-components, by decreasing order of relevance for the AMI. These four correlations indicate the routes by which

21698996, 2022, 16, Downloaded from https://agupubs.onlinelibrary.wiley.com/doi/10.1029/2021JD036392 by Cochrane France, Wiley Online Library on [21/11/2022]. See the Terms and Conditions (https://onlinelibrary.wiley.com/terms-and-conditions) on Wiley Online Library for rules of use; OA articles are governed by the applicable Creative Commons License

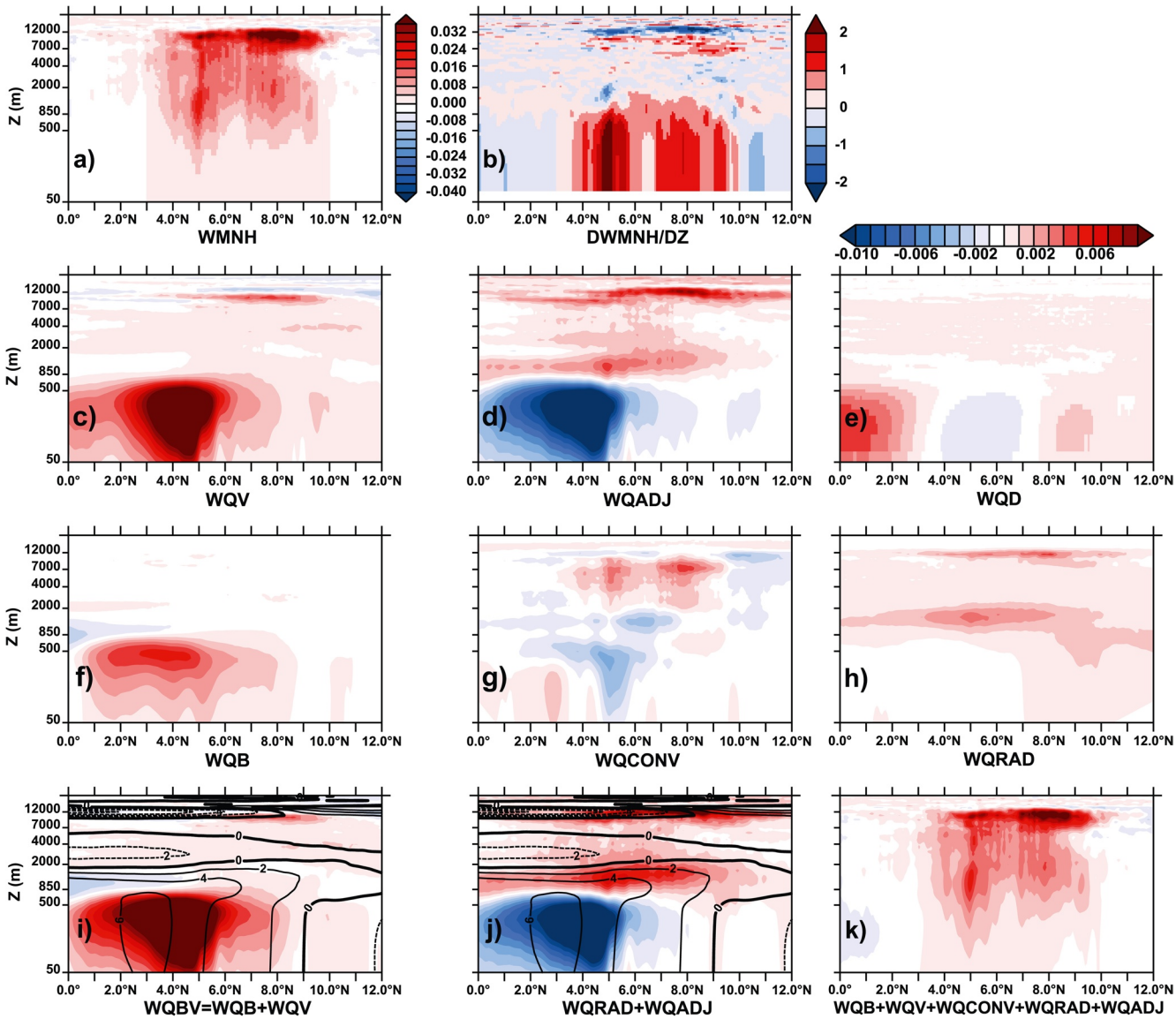


Figure 17. [$y - logz$] cross section at the longitude 20°W of (a) the simulated vertical velocity *WMNH* (m s^{-1}), (b) *WMNH* divergence ($\partial w/\partial z$, s^{-1}) and the vertical velocity components (m s^{-1}) (c) frontogenesis (*WQV*), (d) ageostrophic adjustment (*WQADJ*), (e) turbulent momentum (*WQD*), (f) buoyancy (*WQB*), (g) convection (*WQCONV*), (h) radiation (*WQRAD*), (i) *WQBV* = *WQB* + *WQV*, (j) *WQRAD* + *WQADJ*, (k) *WQB* + *WQV* + *WQCONV* + *WQRAD* + *WQRAD*. Superimposed isolines on Figures (i) and (j) represent the meridional wind (m s^{-1}) highlighting the shallow meridional circulation in the vertical cross section. Figures (c, d, f, g, h, i, j, k) share the colorbar of Figure (a).

FBUO controls the wind convergence in the MABL. The same conclusions were obtained when considering the correlations between the w-components and the Laplacian of surface buoyancy flux, but with opposite signs.

5. Summary and Discussion

The eight *w*-components of the generalized ω-equation based on the **Q**-vectors approach were diagnosed on a validated mesoscale simulation of the AMI during June 2010, in order to identify the physical processes which generate upward motion in the AMI. This study has shown that the combination of all processes is needed to retrieve faithfully the patterns of the vertical velocity. This result points out that the vertical velocity in the AMI results of complex interactions between diabatic and dynamic processes.

21698996, 2022, 16, Downloaded from https://agupubs.onlinelibrary.wiley.com/doi/10.1029/2021JD036392 by Cochrane France, Wiley Online Library on [21/11/2022]. See the Terms and Conditions (https://onlinelibrary.wiley.com/terms-and-conditions) on Wiley Online Library for rules of use; OA articles are governed by the applicable Creative Commons License

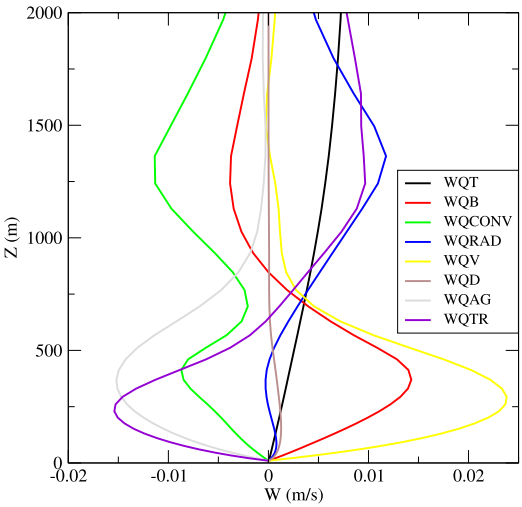


Figure 18. Vertical distributions of vertical velocity components (m s^{-1}) averaged over the AMI domain (see Figure 7).

Diagnostics of *w*-components from inversion of the ω-equation, offer the possibility to propose a conceptual scheme of the vertical dynamics of the AMI. The main sources of upward motion in the AMI distribute on the vertical into three layers, which are:

- MABL (z < 600 m): Frontogenesis *WQV* and buoyancy *WQB* *w*-components balanced by the ageostrophic adjustment *WQADJ* *w*-component
- Layer [600–2,000 m]: Ageostrophic adjustment *WQADJ* and radiative *WQRAD* *w*-components balanced by the deep convection *WQCONV* *w*-component
- Layer [2,000–15,000 m]: Ageostrophic adjustment *WQADJ* and convective *WQCONV* *w*-components

In the MABL (z < 600 m) the sources of upward motions are primarily the frontogenesis mechanism *WQV* and the convergence of buoyancy flux *WQB*, but these processes are mainly regulated by the ageostrophic adjustment *WQADJ*, which is active when residuals **TWI** are not canceled. The MABL balance (*WQV* + *WQB* + *WQADJ*) appeared to be robust since it also well captures latitudinal oscillations of the full vertical velocity and precipitation during June 2010, meaning that boundary-layer processes play a central role in the AMI dynamics. In addition, *WQV* and *WQB* in the MABL were identified as the primary components of the engine of the shallow meridional circulation, which is characterized by a southerly inflow and a strong *w*-divergence below 2,000 m, and a northerly return flow in the layer [2,000–4,000 m], between the equator and 10°*N*.

The existence of a shallow meridional circulation was evidenced in the eastern tropical Pacific (Zhang et al., 2004) from observations collected during the field campaign of EPIC in 2001. Trenberth et al. (2000) also diagnosed shallow circulations in analyses products in other tropical basins. These authors mentioned that the shallow meridional circulations in the tropics may have significant climatic implications through its effects on the MABL properties. The causes of such shallow circulations remain speculative and often argue on the meridional gradient of SST (Lindzen & Nigam, 1987) and momentum entrainment at the top of the MABL (Stevens et al., 2002),

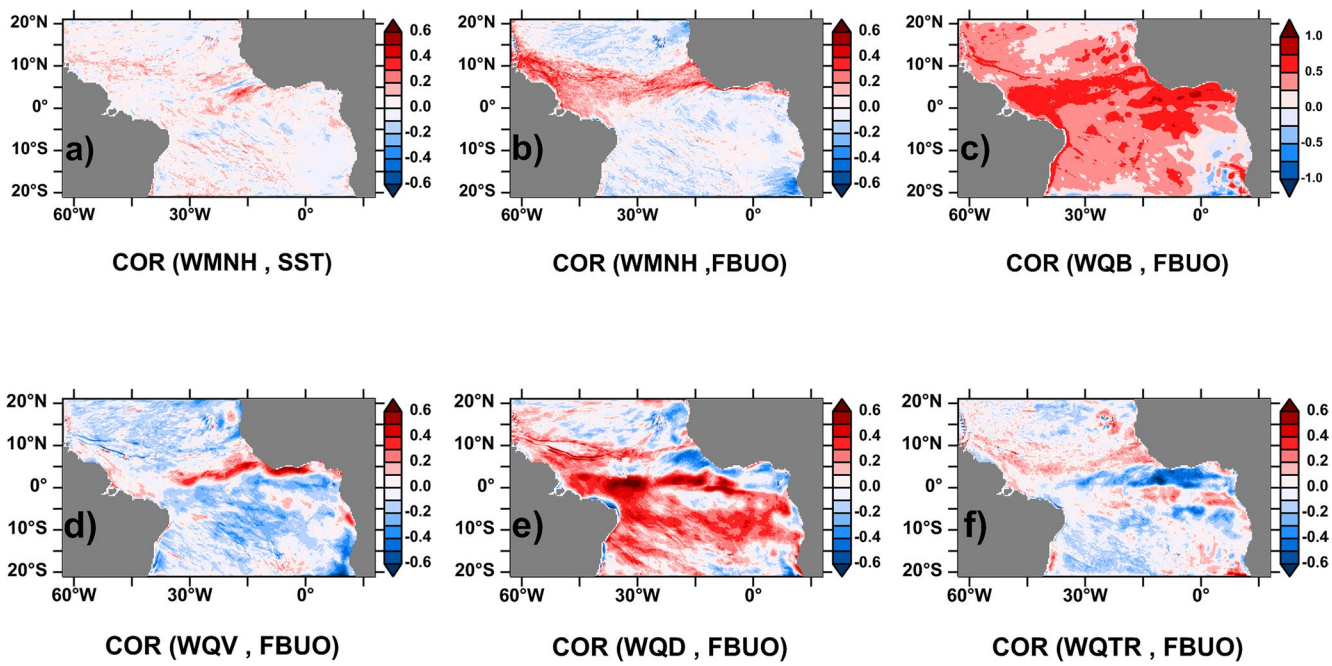


Figure 19. Time correlations of the *w*-components of *WMNH* with the *SST* and the surface buoyancy flux *FBUO*.

21698996, 2022, 16, Downloaded from https://agupubs.onlinelibrary.wiley.com/doi/10.1029/2021JD036392 by Cochrane France, Wiley Online Library on [21/11/2022]. See the Terms and Conditions (https://onlinelibrary.wiley.com/terms-and-conditions) on Wiley Online Library for rules of use; OA articles are governed by the applicable Creative Commons License

21698996, 2022, 16, Downloaded from https://agupubs.onlinelibrary.wiley.com/doi/10.1029/2021JD036392 by Cochrane France, Wiley Online Library on [21/11/2022]. See the Terms and Conditions (https://onlinelibrary.wiley.com/terms-and-conditions) on Wiley Online Library for rules of use; OA articles are governed by the applicable Creative Commons License

which tend to reduce the southerlies. An alternative mechanism might lie in the different response of the atmosphere depending on the height of diabatic heating.

Wu (2003) examined the circulations driven by deep and shallow heatings. His findings show that the temperature perturbation generated by deep convective heating at high levels cannot be amplified because the diabatic heating is rapidly balanced by the adiabatic cooling due to upward motion. The temperature perturbation driven by shallow heating is trapped near the heating area as a consequence, it cannot be balanced by adiabatic cooling through upward motion and a negative temperature gradient forms at the MABL top. In response to this temperature perturbation, a shallow circulation sets up and intensifies the heat source by convergence of buoyancy. Therefore, the system of shallow heating and driven circulation is unstable unless deep convection consumes the excessive low-levels energy. Finally, the circulation driven by deep heating does not feedback on low-level convergence and the deep heating cannot be self-sustaining.

In light of the mechanism proposed by Wu (2003), *WQB* can be viewed as the first dynamic response to the MABL heating which is amplified by convergence of temperature, namely the frontogenesis *WQV*. Our results show that the ageostrophic adjustment *WQADJ* and radiative *WQRAD* forcings propagate the southerly inflow and the associated *w*-divergence above the MABL in the layer [600–2,000 m]. *WQADJ* plays an important role in these low-levels because it acts as a regulator of the forcings *WQB* and *WQV* in the MABL, while it boosts the vertical velocity just above the MABL. This behavior has to be related to the temperature perturbations mentioned by Wu (2003) because it destroys the thermal-wind balance and finally produces **TWI** within the MABL and above it in the wind-shear area. Furthermore, Bretherton et al. (2005) and Nolan et al. (2007) mentioned the strengthening of the shallow circulation by radiation but this forcing was not identified as a driving mechanism. However, Dixit et al. (2008) found that the cloud-induced radiative flux modification affects the lower-level overturning circulation and the width of the ITCZ, in agreement with our results. Note that a negative feedback of the deep convection ($WQCONV < 0$) on the circulation convergence was found below 2,000 m, suggesting that the deep convection acts as a teleconnection from high to low levels.

At high levels, *WQADJ* is also a significant source of upward motion in the TEJ ($z \simeq 12{,}000$ m) in order to counteract the **TWI** induced by convection latent heat release (*WQCONV*). In the free troposphere ([2,000–15,000 m]) our results extend the existing WTG framework in which only the diabatic heating (convection here) and stability determine the vertical velocity. The significance of the adjustment contribution, linked to the ageostrophic circulation and tendency is the main mechanism at stake. It adds a supplementary ascent in the convective core. Dixit et al. (2008) mentioned that surface convergence and the ITCZ is thought to be driven predominantly by boundary-layer processes while by dynamics rather than by thermodynamics processes at high levels in the atmosphere. Our results confirm these propositions, and particularly the strong dynamic contribution *WQDYN* at high levels, mostly through the *WQTR* *w*-component. The Ekman pumping *WQD* was not identified as a major contribution in the MABL at local scale. These results are in agreement with those of Byrne and Thomas (2019) who showed that Ekman pumping is insufficient for estimating vertical velocity close to and within the ITCZ suggesting that non-Ekman dynamical processes need to be accounted for.

Conclusions of studies based on linear idealized models cited in the introduction are in broad accordance with the SST-induced pressure adjustment mechanism and vertical momentum mixing (Sweet et al., 1981), for driving the boundary-layer wind convergence and upward motions in the tropics. This pressure adjustment mechanism is associated with boundary-layer temperature gradients, which are closely related to SST gradients (Lindzen & Nigam, 1987). In our approach the pressure adjustment mechanism is taken into account into the processes involved in the temperature gradient evolution, namely the diabatic (*WQB*, *WQRAD*, *WQCONV*) and frontogenetic (*WQV*) components, while the momentum vertical mixing mechanism is represented by the *WQD* component. The major role of the pressure adjustment in the MABL wind convergence is confirmed by *WQB* and *WQV* in this study but these components give advanced insights into the processes which cause this adjustment. In the literature the pressure adjustment mechanism (Lindzen & Nigam, 1987) refers to the Laplacian of pressure which is driven by the Laplacian of SST or temperature in the MABL (Foussard et al., 2019). Our approach shows why the Laplacian operator is involved in the diagnosis of the vertical velocity $\left(w \propto -\vec{\nabla}.\vec{Q}\right)$, identifies the various diabatic contributions (shallow and deep convection, radiation, diffusion), which alter the pressure, and take into account their vertical distributions, which is usually not the case mainly in simplified approaches. On the other hand, the frontogenesis mechanism, mentioned by Wu (2003) in its academic study, is the main source of upward motion in the present real case, particularly in the southern flank of the AMI. Our findings have also shown that

21698996, 2022, 16, Downloaded from https://agupubs.onlinelibrary.wiley.com/doi/10.1029/2021JD036392 by Cochrane France, Wiley Online Library on [21/11/2022]. See the Terms and Conditions (https://onlinelibrary.wiley.com/terms-and-conditions) on Wiley Online Library for rules of use; OA articles are governed by the applicable Creative Commons License

the ageostrophic adjustment component (*WQADJ*) balances and regulates the diabatic positive components *WQB* and *WQV* in the boundary-layer in order to minimize the **TWI**, in accordance with the Le Chatelier's principle. This negative feedback is an original result not addressed in the literature to our knowledge, while it is also an important forcing at low and high levels. In the Lindzen and Nigam (1987) model, a nonlocal effect of the deep convection heating is specified to limit the boundary-layer wind convergence. This constraint is represented with a back-pressure formulation for free-tropospheric feedbacks on the boundary-layer. In the present study, the back-pressure effects could be attributed to the convective-induced cooling at low levels, resulting in a negative *WQCONV*.

If it is reasonable to expect a direct relationship between the SST, wind convergence and finally convection, an actual relationship between the local SST and the atmospheric circulation over warm oceans is rather complex because of the influence of dynamic and diabatic processes that govern atmospheric circulation in lower and middle troposphere. As consequence, regions of the warmest SST, maximum surface wind convergence are necessarily not collocated (Meenu et al., 2012). In this study time correlations were used to estimate the connections between the boundary-layer vertical velocity to the SST and surface buoyancy flux in the AMI. The correlations revealed a weak control of the SST, excepted where SST gradients are stronger on the northern and southern flanks of the AMI, while a strong control of the surface buoyancy flux on the vertical velocity. Highest correlations, in decreasing order of intensity, are obtained with the *WQB*, *WQV*, *WQTR*, and *WQD* components showing the processes involved in the coupling between the surface buoyancy flux and the boundary-layer circulation. These processes can be viewed as the pathways by which the surface buoyancy flux controls the wind convergence. The diabatic *WQB* component is the straightforward path for this coupling by construction, and the dynamic *WQV*, *WQTR* and *WQD* components are indirect paths associated with surface buoyancy-induced temperature and wind anomalies. These results suggest that surface buoyancy flux has a potential to be more informative than SST in boundary-layer wind convergence and support the idea that the atmospheric moist static energy is a key parameter for driving the atmospheric circulation (Byrne & Thomas, 2019; Chou et al., 2009; Sobel & Neelin, 2006). In particular, Byrne and Thomas (2019) proposed an estimation of the vertical velocity in the ITCZ which scales with the Laplacian of the departure of boundary-layer moist static energy from a critical distribution. This expression is consistent with the diabatic w-component *WQDIAB* and the weak temperature gradient approximation (Sobel et al., 2001) but excludes the dynamics contributions *WQDYN*, which is a significant part of the large-scale circulation (Martin et al., 2016). This study aimed at paving the route to an integrated dynamic and thermodynamic framework to open perspectives toward an unified theory of the ITCZ/AMI. We propose that the generalized ω-equation can be viewed as a general framework that can be used to extend available theories like the WTG approach in the free troposphere and the boundary-layer and to shed light to the connection between the oceanic surface, the boundary-layer and the ITCZ.

Data Availability Statement

All PIRATA data used in this paper are made available for free through the PIRATA main website at https://www.pmel.noaa.gov/gtmba/pmel-theme/atlantic-ocean-pirata. The monthly averaged simulation data are available at https://doi.org/10.5281/zenodo.6542764.

Acknowledgments
The authors acknowledge all the key contributors to the PIRATA program from its inception, that is, the institutions NOAA, IRD, Météo-France, Instituto Nacional de Pesquisas Espaciais, and DHN; all past members of the PIRATA Resources Board and of the PIRATA Scientific Steering Group; all engineers and technicians ensuring the yearly cruises, data acquisition, data treatment, and material maintenance (of NOAA, DHN, and IRD's IMAGO service unit); and Research Vessel crews. We thank two anonymous reviewers for fruitful discussions on the WTG concept and for several important suggestions. This work is dedicated to my mother Rose Inzucchi-Giordani who passed away on August 17, 2021.

References

Back, L., & Bretherton, C. (2009). On the relationship between SST gradients, boundary layer winds, and convergence over the tropical oceans. *Journal of Climate*, *22*, 4182–4196. https://doi.org/10.1175/2009JCLI2392.1

Bechtold, P., Bazile, E., Guichard, F., Mascart, P., & Richard, E. (2001). A mass-flux convection scheme for regional and global models. *Quarterly Journal of the Royal Meteorological Society*, *127*, 869–886.

Belamari, S. (2005). *Report on uncertainty estimates of an optimal bulk formulation for turbulent fluxes, Toulouse, France* (Technical Report 31057). CNRM. MERSEA Integrated Project.

Bischoff, T., & Schneider, T. (2014). Energeticc constraints on the position of the intertropical convergence zone. *Journal of Climate*, *27*, 4937–4951. https://doi.org/10.1175/JCLI-D-13-00650.1

Bougeault, P., & Lacarrère, P. (1989). Parameterization of orography-induced turbulence in a meso-beta scale model. *Monthly Weather Review*, *117*, 1872–1890. https://doi.org/10.1175/1520-0493(1989)117<1872:POOITI>2.0.CO;2

Bourlès, B., Araujo, M., McPhaden, M., Brandt, P., Foltz, G., Lumpkin, R., et al. (2019). PIRATA: A sustained observing system for tropical Atlantic climate research and forecasting. *Earth and Space Science*, *6*, 577–616. https://doi.org/10.1029/2018EA000428

Bretherton, C., Blossey, P. N., & Khairoutdinov, M. (2005). An energy-balance analysis of deep convective self-aggregation above uniform SST. *Journal of the Atmospheric Sciences*, *62*, 4273–4292. https://doi.org/10.1175/jas3614.1

Byrne, M., & Thomas, R. (2019). Dynamics of the ITCZ width: Ekman processes, non-Ekman processes, and links to sea surface temperature. *Journal of the Atmospheric Sciences*, *76*, 2869–2884. https://doi.org/10.1175/jas-d-19-0013.1

Caniaux, G., & Redelsperger, J. (1994). A numerical study of the stratiform region of a fast-moving squall line. Part I: General description and water and heat budgets. *Journal of the Atmospheric Sciences*, *51*, 2046–2074. https://doi.org/10.1175/1520-0469(1994)051<2046:ANSOTS>2.0.CO;2

Carpenter, K. (1982). Radiation conditions for lateral boundaries of limited area numerical models. *Quartely Journal of Royal Meteorological Society*, *110*, 717–719. https://doi.org/10.1002/qj.49710845714

Chiang, J., & Zebiak, S. (2000). Surface wind over tropical oceans: Diagnosis of the momentum balance, and modeling the linear friction coefficient. *Journal of Climate*, *13*, 1733–1747. https://doi.org/10.1175/1520-0442(2000)013<1733:SWOTOD>2.0.CO;2

Chou, C., Neelin, J., Chen, C.-A., & Tu, J.-Y. (2009). Evaluating the "rich-get-richer" mechanism in tropical precipitation change under global warming. *Journal of Climate*, *22*, 1982–2005. https://doi.org/10.1175/2008JCLI2471.1

Crespo, L., Keenlyside, N., & Koseki, S. (2019). The role of sea surface temperature in the atmospheric seasonal cycle of the equatorial Atlantic. *Climate Dynamics*, *52*, 5927–5946. https://doi.org/10.1007/s00382-018-4489-4

Cuxart, J., Bougeault, P., & Redelsperger, J. (2000). A turbulence scheme allowing for mesoscale and large-eddy simulations. *Quarterly Journal of Royal Meteorological Society*, *126*, 1–30. https://doi.org/10.1002/qj.49712656202

Davies, H. (1976). A lateral boundary formulation for multi-level prediction models. *Quartely Journal of Royal Meteorological Society*, *102*, 405–418. https://doi.org/10.1002/qj.49710243210

Diakhaté, M., Lazar, A., Coëtlogon, G. D., & Gaye, A. (2018). Do SST gradients drive the monthly climatological surface wind convergence over the tropical Atlantic? *International Journal of Climatology*, *38*, 955–965. https://doi.org/10.1002/joc.5422

Dixit, V., Geoffroy, O., & Sherwood, S. C. (2008). Control of ITCZ width by low-level radiative heating from upper-level clouds in aquaplanet simulations. *Geophysical Research Letters*, *45*, 5788–5797. https://doi.org/10.1029/2018GL078292

Doi, T., Vecchi, G., Rosati, A., & Delworth, T. (2012). Biases in the Atlantic ITCZ in seasonal-interannual variations for a Coarse- and a Heigh-resolution coupled climate model. *Journal of Climate*, *25*, 5494–5511. https://doi.org/10.1175/JCLI-D-11-00360.1

Durran, D. (1989). Improving the anelastic approximation. *Journal of the Atmospheric Sciences*, *46*, 1453–1461. https://doi.org/10.1175/1520-0469(1989)046<1453:ITAA>2.0.CO;2

Foussard, A., Lapeyre, G., & Plougonven, R. (2019). Response of surface wind divergence to mesoscale SST anomalies under different wind conditions. *Journal of the Atmospheric Sciences*, *76*, 2065–2082. https://doi.org/10.1175/JAS-D-18-0204.1

Giordani, H., & Caniaux, G. (2014). Lagrangian sources of frontogenesis in the equatorial Atlantic. *Frontiers in Climate Dynamics*, *43*(11), 3147–3162. https://doi.org/10.1007/s00382-014-2293-3

Giordani, H., & Planton, S. (2000). Modeling and analysis of ageostrophic circulation over the Azores oceanic front during the SEMAPHORE Experiment. *Monthly Weather Review*, *128*, 2270–2287. https://doi.org/10.1175/1520-0493(2000)128<2270:MAAOAC>2.0.CO;2

Giordani, H., Prieur, L., & Caniaux, G. (2006). Advanced insights into sources of vertical velocity in the ocean. *Ocean Dynamics*, *56*, 513–524. https://doi.org/10.1007/s10236-005-0050-1

Herman, M., & Raymond, D. (2014). WTG cloud modeling with spectral decomposition heating. *Journal of Advances in Modeling Earth Systems*, *6*, 1121–1140. https://doi.org/10.1002/2014MS000359

Holton, J., & Hakim, G. (2013). *An introduction to dynamic meteorology* (5th ed., p. 511). Academic Press. https://doi.org/10.1016/C2009-0-63394-8

Hoskins, B., Draghici, I., & Davies, H. (1978). A new look at the *w*-equation. *Quarterly Journal of Royal Meteorological Society*, *104*, 31–38. https://doi.org/10.1002/qj.49710443903

Janicot, S., Caniaux, G., Chauvin, F., de Cotlogon, G., Fontaine, B., Hall, N., et al. (2011). Intraseasonal variability of the West African monsoon. *Atmospheric Science Letters*, *12*, 58–66. https://doi.org/10.1002/asl.280

Kain, J., & Fritsch, J. (1993). Convective parameterization for mesoscale models: The Kain-Fritsch scheme. The representation of cumulus convection in numerical models. *Meteorological Monographs*, *24*, 165–170. https://doi.org/10.1007/978-1-935704-13-3_16

Kang, S., & Held, I. (2012). Tropical precipitation, SSTs and the surface energy budget: A zonally symmetric perspective. *Climate Dynamics*, *38*, 1917–1924. https://doi.org/10.1007/s00382-011-1048-7

Klemp, J., & Wilhelmson, R. (1978). The simulation of three-dimensional convective storm dynamics. *Journal of the Atmospheric Sciences*, *35*, 1070–1096. https://doi.org/10.1175/1520-0469(1978)035<1070:TSOTDC>2.0.CO;2

Krishnamurti, T. (1968). A diagnostic balance model for studies of weather systems of low and high latitudes, Rossby number less than 1. *Monthly Weather Review*, *17*, 197–207.

Lac, C., Chaboureau, J.-P., Masson, V., Pinty, J.-P., Tulet, C., Escobar, J., et al. (2018). Overview of the meso-nh model version 5.4 and its applications. *Geoscientific Model Development*, *11*, 1929–1969. https://doi.org/10.5194/gmd-11-1929-2018

Lafore, J., Stein, J., Asencio, N., Bougeault, P., Ducrocq, V., Duron, J., & de Arellano, J. V.-G. (1998). The Meso-NH atmospheric simulation system. Part I: Adiabatic formulation and simulations. *Annales Geophysicae*, *16*, 90–109. https://doi.org/10.1007/s00585-997-0090-6

Lamb, P., Peppler, R., & Hastenrath, S. (1986). Interannual variability in the tropical Atlantic. *Nature*, *322*, 238–239. https://doi.org/10.1038/322238a0

Lindzen, R., & Nigam, S. (1987). On the role of sea surface temperature gradients in forcing low level winds and convergence in the tropics. *Journal of the Atmospheric Sciences*, *44*, 2418–2436. https://doi.org/10.1175/1520-0469(1987)044<2418:OTROSS>2.0.CO;2

Mahfouf, J., & Noilhan, J. (1996). The ISBA land surface parameterization scheme. *Global and Planetary Change*, *13*, 145–159. https://doi.org/10.1016/0921-8181(95)00039-9

Marengo, J. A., Soares, W., & Rodriguez, D. (2013). Two contrasting severe seasonal extremes in tropical south Atlantic in 2012: Flood in Amazonia and drought in northeast Brazil. *Journal of Climate*, *26*, 9137–9154. https://doi.org/10.1175/JCLI-D-12-00642.1

Martin, G., Peyrillé, P., Roehrig, R., Rio, C., Caian, M., Bellon, G., et al. (2016). Understanding the West African Monsoon from the analysis of diabatic heating distribution as simulated by climate models. *Journal of Advances in Modeling Earth Systems*, *9*, 239–270. https://doi.org/10.1002/2016MS000697

Masson, V., Champeaux, J.-L., Chauvin, C., Meriguet, C., & Lacaze, R. (2003). A global database of land surface parameters at 1 km resolution in meteorological and climate models. *Journal of climate*, *16*, 1261–1282.

McGauley, M., Zhang, C., & Bond, N. (2004). Large-scale characteristics of the atmospheric boundary layer in the eastern pacific cold tongue/ITCZ region. *Journal of Climate*, *17*, 3907–3920. https://doi.org/10.1175/1520-0442(2004)017<3907:LCOTAB>2.0.CO;2

Meenu, S., Parameswaran, K., & Rajeev, K. (2012). Role of sea surface temperature and wind convergence in regulating convection over the tropical Indian Ocean. *Journal of Geophysical Research*, *117*, D14102. https://doi.org/10.1029/2011JD016947

Meynadier, R., Coëtlogon, G. D., Leduc-Leballeur, M., Eymard, L., & Janicot, S. (2016). Seasonal influence of the sea surface temperature on the low atmospheric circulation and precipitation in the eastern equatorial Atlantic. *Climate Dynamics*, *47*, 1127–1142. https://doi.org/10.1007/s00382-015-2892-7

21698996, 2022, 16, Downloaded from https://agupubs.onlinelibrary.wiley.com/doi/10.1029/2021JD036392 by Cochrane France, Wiley Online Library on [21/11/2022]. See the Terms and Conditions (https://onlinelibrary.wiley.com/terms-and-conditions) on Wiley Online Library for rules of use; OA articles are governed by the applicable Creative Commons License

Mischell, E., & Lee, J.-E. (2022). Observed zonal variations of the relationship between ITCZ position and meridional temperature contrast. *Climate*, *10*, 30. https://doi.org/10.3390/cli10030030

Morcrette, J. (1991). Radiation and cloud radiative properties in the ECMWF forecasting system. *Journal of Geophysical Research*, *96*, 9121–9132. https://doi.org/10.1029/89JD01597

Neelin, J. (1989). On the interpretation of the gill model. *Journal of the Atmospheric Sciences*, *46*, 2466–2468. https://doi.org/10.1175/1520-0469(1989)046<2466:OTIOTG>2.0.CO;2

Nie, J., & Sobel, A. (2016). Modeling the interaction between quasigeostrophic vertical motion and convection in a single column. *Journal of the Atmospheric Sciences*, *73*, 1101–1115. https://doi.org/10.1175/JAS-D-15-0205.1

Nolan, D., Zhang, C., & Chen, S.-H. (2007). Dynamics of the shallow meridional circulation around intertropical convergence zones. *Journal of the Atmospheric Sciences*, *64*, 2262–2285. https://doi.org/10.1175/JAS3964.1

Okumura, Y., & Xie, S. (2004). Interaction of the Atlantic equatorial cold tongue and the African monsoon. *Journal of Climate*, *17*, 3589–3602. https://doi.org/10.1175/1520-0442(2004)017<3589:IOTAEC>2.0.CO;2

Pascual, A., Gomis, D., Haney, R., & Ruiz, S. (2004). A quasigeostrophic analysis of a meander in the Palamós canyon: Vertical velocity, geopotential tendency, and a relocation technique. *Journal of Physical Oceanography*, *34*, 2274–2287. https://doi.org/10.1175/1520-0485(2004)034<2274:AQAOAM>2.0.CO;2

Pauley, P., & Nieman, S. (1992). A comparison of quasigeostrophic and nonquasigeostrophic vertical motions for a model-simulated rapidly intensifying marine extratropical cyclone. *Monthly Weather Review*, *120*(7), 1108–1134. https://doi.org/10.1175/1520-0493(1992)120<1108:ACOQAN>2.0.CO;2

Peyrillé, P., Lafore, J.-P., & Boone, A. (2016). The annual cycle of the west African monsoon in a two-dimensional model: Mechanisms of the rain-band migration. *Quarterly Journal of Royal Meteorological Society*, *142*, 1473–1489. https://doi.org/10.1002/qj.2750

Pietri, A., Capet, X., d'Ovidio, F., Levy, M., Sommer, J. L., Molines, J., & Giordani, H. (2021). Skills and limitation of omega-equation in different oceanic flow regimes. *Journal of Physical Oceanography*, *51*, 931–954. https://doi.org/10.1175/jpo-d-20-0052.1

Pinty, J., & Jabouille, P. (1998). A mixed-phase cloud parameterization for use in a mesoscalenon-hydrostaticmodel: Simulations of a squall line and of orographic precipitation. In *Conference on cloud physics* (pp. 217–220). American Meteorological Society.

Räisänen, J. (1995). Factors affecting synoptic-scale vertical motions: A statistical study using a generalized omega equation. *Monthly Weather Review*, *123*(8), 2447–2460.

Ruiz, S., Pascual, A., Garau, B., Pujol, I., & Tintoré, J. (2009). Vertical motion in the upper ocean from glider and altimetry data. *Geophysical Research Letters*, *36*, L14607. https://doi.org/10.1029/2009GL038569

Samanta, D., Karnauskas, K., & Goodkin, N. (2019). Tropical pacific and ITCZ biases in climate models: Double trouble for future rainfall projections. *Geophysical Research Letters*, *46*, 2242–2252. https://doi.org/10.1029/2018GL081363

Schneider, T., Bischoff, T., & Haug, G. (2014). Migrations and dynamics of the intertropical convergence zone. *Nature*, *513*, 45–53. https://doi.org/10.1038/nature13636

Silva, T., Veleda, D., Araujo, M., & Tyaquica, P. (2018). Ocean-atmosphere feedback during extreme rainfall events in eastern Northeast Brazil. *Journal of Applied Meteorological and Climatology*, *57*, 1211–1229. https://doi.org/10.1175/JAMC-D-17-0232.1

Sobel, A., & Neelin, J. (2006). The boundary layer contribution to intertropical convergence zones in the quasi-equilibrium tropical circulation model framework. *Theoretical and Computational Fluid Dynamics*, *20*, 323–350. https://doi.org/10.1007/s00162-006-0033-y

Sobel, A., Nilsson, J., & Polvani, L. M. (2001). The weak temperature gradient approximation and balanced tropical moisture waves. *Journal of the Atmospheric Sciences*, *58*, 3650–3665. https://doi.org/10.1175/1520-0469(2001)058<3650:TWTGAA>2.0.CO;2

Sodré, G., & Filho, J. S. (2013). Eestudo de caso: Análise sinótica de um evento extremo de precipitac*tildeao* no estado de pernambuco entre os dias 17 e 19 de junho de 2010. *Revista Brasileira de Geografia*, *6*, 66–78. https://doi.org/10.26848/rbgf.v6i1.232820

Stepanyuk, O., Riäisänen, J., Sinclair, V. A., & Jrvinen, H. (2017). Factors affecting atmospheric vertical motions as analyzed with a generalized omega equation and the OpenIFS model. *Tellus*, *69*, 1271563. https://doi.org/10.1080/16000870.2016.1271563

Stevens, B., Duan, J., McWilliams, J., Munnich, M., & Neelin, J. (2002). Entrainment, Rayleigh friction, and boundary layer winds over the tropical Pacific. *Journal of Climate*, *15*, 30–44. https://doi.org/10.1175/1520-0442(2002)015<0030:ERFABL>2.0.CO;2

Sultan, B., & Janicot, S. (2003). The West African monsoon dynamics. Part II: The 'preonset' and 'onset' of the summer monsoon. *Journal of Climate*, *16*, 3407–3427. https://doi.org/10.1175/1520-0442(2003)016<3407:TWAMDP>2.0.CO;2

Sweet, W., Fett, R., Kerling, J., & Violette, P. L. (1981). Air-sea interaction effects in the lower troposphere across the north Wall of the Gulf Stream. *Monthly Weather Review*, *109*, 1042–1052. https://doi.org/10.1175/1520-0493(1981)109<1042:ASIEIT>2.0.CO;2

Thorncroft, C., Nguyen, H., Zhang, C., & Peyrillé, P. (2011). Annual cycle of the west African monsoon: Regional circulations and associated water vapour transport. *Quarterly Journal of Royal Meteorological Society*, *137*, 129–147. https://doi.org/10.1002/qj.728

Trenberth, K., Stepaniak, D. & Caron, J. M. (2000). The global monsoon as seen through the divergent atmospheric circulation. *Journal of Climate*, *13*(22), 3969–3993.

Viùdez, A., Tintoré, J., & Haney, R. (1996). About the nature of the generalized omega equation. *Journal of the Atmospheric Sciences*, *53*, 787–795. https://doi.org/10.1175/1520-0469(1996)053<0787:ATNOTG>2.0.CO;2

Voldoire, A., Exarchou, E., Sanchez-Gomez, E., Demissie, T., Deppenmeier, A.-L., Frauen, C., et al. (2019). Role of wind stress in driving SST abiases in the tropical Atlantic. *Climate Dynamics*, *53*, 3481–3504. https://doi.org/10.1007/s00382-019-04717-0

Wahl, S., Latif, M., & Park, W. (2009). On the tropical Atlantic SST warm bias in the Kiel climate model. *Climate Dynamics*, *36*, 891–906. https://doi.org/10.1007/s00382-009-0690-9

Wang, B., & Li, T. (1993). A simple tropical atmospheric model of relevance to short-term climate variations. *Journal of the Atmospheric Sciences*, *50*(2), 2017–2027. https://doi.org/10.1175/1520-0469(1993)050<0260:ASTAMO>2.0.CO;2

Wang, Y., Heywood, K., Stevens, D., & Damerell, G. (2021). Seasonal extrema of sea surface temperature in CMIP6 models. *Ocean Science*, *18*, 839–855. https://doi.org/10.5194/os-2021-102

Wu, Z. (2003). A shallow CISK, deep equilibrium mechanism for the interaction between large-scale convection and large-scale circulation in the tropics. *Journal of the Atmospheric Sciences*, *60*, 377–392. https://doi.org/10.1175/1520-0469(2003)060<0377:ASCDEM>2.0.CO;2

Zebiak, S. (1982). A simple atmospheric model of relevance to El Nio. *Journal of the Atmospheric Sciences*, *39*(9), 2017–2027. https://doi.org/10.1175/1520-0469(1982)039<2017:ASAMOR>2.0.CO;2

Zhang, C., McGauley, M., & Bond, N. (2004). Shallow meridional circulation in the tropical eastern pacific. *Journal of Climate*, *17*, 133–139. https://doi.org/10.1175/1520-0442(2004)017<0133:SMCITT>2.0.CO;2

21698996, 2022, 16, Downloaded from https://agupubs.onlinelibrary.wiley.com/doi/10.1029/2021JD036392 by Cochrane France, Wiley Online Library on [21/11/2022]. See the Terms and Conditions (https://onlinelibrary.wiley.com/terms-and-conditions) on Wiley Online Library for rules of use; OA articles are governed by the applicable Creative Commons License